ABSTRACT

PROTON SPIN FLIP PROBABILITY IN INELASTIC SCATTERING ON ^{120}Sn AND ^{124}Sn AT 30 MeV

By

Richard Harry Howell

Proton spin-flip in the excitation of the first 2^+ states in ^{120}Sn and ^{124}Sn has been measured at 30 MeV using the (p,p'γ) coincidence technique. The data are fit by the DWA collective model using the full Thomas spin-orbit coupling term and by the DWA microscopic model using detailed wave functions and a realistic interaction. These calculations are also compared to published proton angular distribution and asymmetry data on the first excited state in ^{120}Sn at 30 MeV. The effect of including a realistic two body spin-orbit interaction was investigated with respect to these data. The effect of complex coupling was also investigated for these data and published cross section and asymmetry data on the first excited states of ^{208}Pb and ^{58}Ni. Imaginary form factors obtained from the collective model and from a phenomenological microscopic prescription were used. It is concluded that an imaginary term in the form factor can be important.

PROTON SPIN FLIP PROBABILITY IN INELASTIC SCATTERING ON ^{120}Sn AND ^{124}Sn AT 30 MeV

by

Richard Harry Howell

A THESIS

Submitted to
Michigan State University
in partial fulfillment of the requirements
for the degree of

DOCTOR OF PHILOSOPHY

Department of Physics

1972

ACKNOWLEDGEMENTS

As are many doctoral students at the MSU Cyclotron Laboratory, I am indebted to the entire Cyclotron staff for their ready assistance during the course of this work.

I wish to thank Professor H. McManus, Dr. F. Petrovitch and G. R. Hammerstein for their assistance and encouragement in performing theoretical calculations and to R. Frick for assistance in running the codes.

I am grateful to M. Savoie and R. Doering for the many nights spent assisting in the collection of the data.

I am happy to thank Mrs. Mary Krueger for her cheerful assistance both in the computer room and in typing this dissertation.

Finally and especially, I am indebted to Professor A. Galonsky. His advice, assistance, and encouragement were most valuable during my tenure at MSU.

TABLE OF CONTENTS

2. Nuclear Theory

3. Experimental Procedure

4. Data Analysis

LIST OF TABLES

LIST OF FIGURES

1. INTRODUCTION

In order to learn about the spin-dependent part of the interaction in an inelastic scattering reaction there are various measurements possible. The angular distribution of the differential cross section, asymmetry, polarization and in special cases the projectile spin flip may all be measured.

The probability of a spin-flip event occurring may be measured through the particle-de-excitation gamma-ray angular correlation function with the gamma-ray detector fixed perpendicular to the scattering plane. Measurements of the angular distribution of the spin flip probability of scattered protons have been reported on the lowest 2^+ states of several even-even targets with mass numbers ranging from 12 to 64 and incident proton energies ranging from 10 to 40 MeV. There are also spin flip data reported on some of these targets for the scattering of medium energy helions and deuterons.

This report shows angular distributions for the proton spin flip probability taken on the lowest 2^+ states in ^{120}Sn and ^{124}Sn at 30 MeV bombarding energy. The data were compared with calculations done in the Distorted Wave Approximation. Asymmetries and cross sections were calculated and compared with data on ^{120}Sn taken elsewhere at the same energy (KA 70).

The four measured quantities, cross section, asymmetry, polarization and spin flip, are related to the set of partial cross sections corresponding to specific entering and exiting projectile spin projections along the normal to the scattering plane. These may be written:

Cross section

$$\sigma = \sigma_{++} + \sigma_{+-} + \sigma_{-+} + \sigma_{--}$$

Asymmetry

$$\sigma A = \sigma_{++} + \sigma_{+-} - \sigma_{-+} - \sigma_{--}$$

Polarization

$$\sigma P = \sigma_{++} - \sigma_{+-} + \sigma_{-+} - \sigma_{--}$$

Spin flip

$$\sigma S = \sigma_{+-} + \sigma_{-+} \qquad (1.1)$$

The symbol subscripts +- denote incoming projection + and exiting projection -. The cross section may be measured using an unpolarized beam by detecting the number of scattered particles in some solid angle. The cross section is: differential cross section = number of scattered particles / (number scattering centers x number of incoming particles x solid angle). The asymmetry is measured with a polarized beam by detecting the difference in the number of particles scattered into the same solid angle at scattering angles + and - θ. The difference is then normalized to the sum of the scattered counts to obtain the asymmetry. The polarization is measured with an unpolarized beam by measuring the difference between the number of spin up and spin down particles scattered into some solid angle. This difference normalized to the sum of the scattered counts is the polarization.

The measurement of the spin-flip probability through the proton gamma-ray correlation function is deduced with the aid of the Bohr Theorem (BO 59). This theorem is model independent, depending only on reflection symmetry in the reaction plane for its derivation. It may be simply stated $\Delta M_S + \Delta M_J = + / -$ as the change in parity in the reaction is even/odd, ΔM_S (ΔM_J) is the change in the projection of the projectile (target) spin along an axis normal to the scattering plane, the Z axis. In the case of a $J = 0$ initial target state, information about the behavior of the projectile spin projection during the reaction is retained in the population of the sublevels in the excited target state. During the radiative decay, only $|\Delta M_J| = 1$ transitions are non-zero along the Z axis (SH 70). Thus for 0^+ to 1^+ and 0^+ to 2^+ inelastic scattering, a projectile spin-flip will always produce a de-excitation gamma-ray radiation pattern which is clearly separated along the Z axis from the radiation from non-spin-flip events. For higher spins $|\Delta M| \geq 3$ channels are also open for de-excitation of sublevels populated by spin-flip. The de-excitation gamma-ray radiation patterns from some excited state contain the most useful information about the excited substates for decays to a $J = 0$ ground state where the substate quantum numbers retain a unique correspondence with the magnetic quantum numbers of the transition operator. Thus all measurements reported to date have been done on the first excited 2^+ state of an even-even target nucleus. Also, lower mass targets are preferred on experimental grounds, as the ratio of the gamma-ray yield from the first excited state to the total gamma-ray yield is higher and the energy of the state is generally high. The lightest isotope studied has been C^{12} at 10.3 MeV (SC 64), 12 - 20 MeV (KO 69B), 15.9 and 17.5 MeV (WI 71), and 26.2 and 40 MeV (KO 69A). In the s-d shell, Mg^{24} has been done at 10.3 MeV (SC 64), Si^{28} at 30 and 40 MeV (GI 68) and S^{32} at 15.5 and 17.9 MeV (WI 71). Heavier isotopes studied include Fe^{54} at 10 MeV (AH 70); Fe^{54} and Fe^{56} at 19.6 MeV (HE 69); Cr^{50} and Cr^{52} at 12 MeV (SW 71) and a great amount of data due to the University of Washington group on Ni^{58} at 10.3 MeV (SC 64), 9.25 - 20 MeV (KO 69B) and 20 MeV (EE 71); Ni^{60} at 10 MeV (AH 70); Ni^{60} and Ni^{64} at 10.5 and 14 MeV (KO 69B). Thus the presentation of data on Sn^{120} and Sn^{124} at 30 MeV considerably extends the range in mass of isotopes studied.

Data have been taken with other beams. He^3 spin flip is reported on C^{12} at 22.5 MeV (PA 68). Deuteron half spin flip ($\Delta M_s = \pm 1$) has been reported for $^{24,26}Mg$, ^{32}S, $^{48,50}Ti$, $^{58,60}Ni$ at 11.8 MeV (HI 70).

With the exception of some data taken at energies for which compound nuclear effects are important, all the above data show the same general features. First, in every case there is a large peak from .3 to .4 in magnitude which dominates the spin flip probability angular distribution. This peak occurs at back angles with a maximum at around 150° proton scattering angle. Collective model calculations which normally have not included any spin transfer in the nuclear interaction fit this back angle peak in most cases. In all cases a back angle peak is predicted. The collective model sometimes fails in fitting the height of the peak. This is usually associated with a failure of the optical model in fitting the elastic scattering and polarization data. A second general feature of these data is a uniformly low, less than .1, and smoothly varying angular distribution at angles forward of around 100° proton scattering angle with a small peak at about 75°. Exceptions to this tendency do occur. In some reported data, the second peak is seen in the general vicinity of 90°. This peak with a magnitude of about .2 is not as large as the back angle peak and is not always predicted in collective model calculations.

The collective model calculations are only dependent on the values of the optical model parameters. The general success of the collective model in fitting spin-flip probabilities over such a wide range of target mass and energy suggests that the dominant processes producing a spin-flip are dependent on the optical (distorted wave) channels in the spin-flip scattering. An attempt has been made to use this property to determine a value for the optical spin-orbit well depth in ^{3}He scattering from C^{12} (PA 68). Proton scattering from C^{12} and S^{32} have been studied and the optical model parameters adjusted in an attempt to fit both spin flip and elastic data (WI 71).

In Figure 1.1 the collected data for all targets at all energies for which direct reactions are dominant are displayed. The uniform character of the spin flip angular distribution is easily seen in this figure.

The spin flip data on ^{120}Sn and ^{124}Sn reported in this thesis are typical of those data just described. The increase in the mass of these targets over that of previous targets does not significantly change the character of the data. A small isotopic effect appears at angles forward of 75° proton scattering angle. In this region the values from ^{120}Sn are consistently higher than those from ^{124}Sn. DWA collective model calculations including a full Thomas distorted spin orbit term (SH 68) fit these data well. Varying the spin orbit deformation from 0 to twice the deformation of the central well did not greatly affect the quality of these fits. Comparisons with published asymmetry data were more sensitive to the spin orbit deformation. They indicate that the spin orbit and central deformations should be about the same. Microscopic calculations using the tin wave functions of D. M. Clement and E. Baranger (CL 68) and the Kallio-Kolltveit force also fit the spin flip well. The real, central Kallio-Kolltveit force predicts the asymmetry badly. An

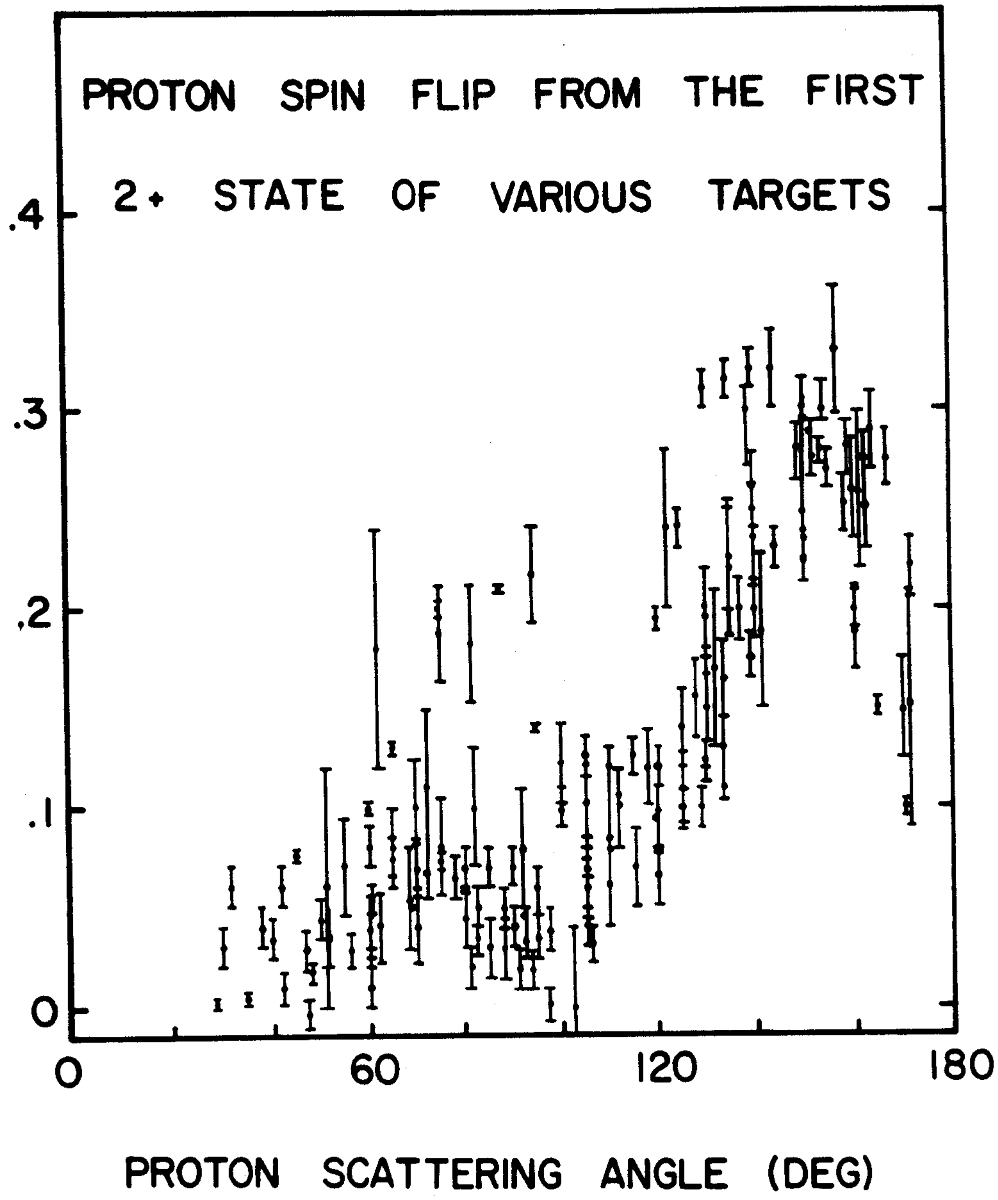

Figure 1.1 Proton spin-flip on targets ranging from ^{12}C to ^{60}Ni at beam energies from 15 to 40 MeV.

imaginary contribution was estimated. The quality of the asymmetry fit was greatly improved by this addition. The fit to the cross section was also somewhat improved.

2. NUCLEAR THEORY

2.1 Approximations in the Treatment of Scattering

Reactions which occur in a time interval comparable to the transit time across a nucleus are often thought of as direct reactions. The theoretical treatment of these reactions in the plane wave approximation is outlined by Tobocman (TO 61). In this approximation, the interaction potential is treated as a perturbation and the incident and exiting particle wave functions are plane waves. A more complicated approximation separates the elastic scattering interaction potential from the total interaction potential. The incoming and exiting channels are then described by the wave functions for elastic scattering. This is the distorted wave approximation (DWA). The algebra of this approximation has been discussed by G. R. Satchler (SA 64). A brief discription of the DWA, methods for treating polarization phenomena in the DWA and the use of some nuclear models in the DWA are found in the following sections. DWA calculations were performed with DWMAIN, a code written by T. Tamura and R. M. Haybron at ORNL and modified at M.S.U. and a collective model DWA code written by H. Sherif at the University of Washington

2.2 Optical Model

In order to accomplish the more sophisticated calculations of the DWA prescription, elastic scattering wave functions must be calculated which are a more accurate description of the scattering than that of plane waves.

To describe elastic scattering and polarization of protons, a phenomenological scattering potential has been developed. The strength and shape of this potential has been parameterized. Searches are made on the potential parameters attempting to minimize the chi-squared values of calculated and experimental elastic cross sections and polarizations.

The experience of a great many researchers in applying this model to a wide variety of elastic scattering data has resulted in a successful potential form which has become accepted in describing proton elastic scattering.

The accepted optical model scattering potential in use for the elastic scattering of protons at this time is

$$U(r) = V(r) + iW(r) \tag{2.1}$$

where

$$\begin{aligned} V(r) = {} & V_c(r) - V_R\, f(r, R_R, a_R) \\ & + V_{so}\left(\frac{\hbar}{m_\pi c}\right)^2 \vec{\sigma}\cdot\vec{\ell}\, \frac{1}{r}\frac{d}{dr} f(r, R_{so}, a_{so}) \end{aligned}$$

and

$$W(r) = -W_V\, f(r,\, R_I',\, a_I',)$$

$$+\, W_{SF}\, 4a_I \frac{d}{dr} f(r,\, R_I,\, a_I)$$

The Coulomb potential, V_c, is normally taken to be the potential between a point charge, ez, and a sphere of uniform charge, Ze and radius R_c. Thus

$$V_c = \begin{cases} \frac{Zze^2}{2R_c} \left[3 - \frac{r}{R_c}^2\right], & r \leq R_c \\ \frac{Zze^2}{r}, & r > R_c \end{cases} \qquad (2.2)$$

The radial functions f(r, R, a) are of the Woods-Saxon (Fermi) form

$$f(r,\, R,\, a) = [1 + \exp\,(r - R)\, /\, a]^{-1} \qquad (2.3)$$

The nuclear radius R is further factored into $R_x = r_x A^{1/3}$ where A is the atomic mass number of the nucleus. The notation used here is consistent with that of F. D. Becchetti and G. W. Greenless (BE 69).

The distorted waves used in DWA calculations of inelastic proton scattering are obtained from a potential of this form. Also small deformations from the spherical shape of this potential are expected in a macroscopic picture of an excited nuclear state. Thus in the macroscopic (collective) model of inelastic scattering, the scattering interaction potential may be deduced from the optical model potential.

2.3 DWA Basic Formalism

Using the notation A(a,b)B, the differential cross section is written

$$\frac{d\sigma}{d\Omega} = \frac{\mu_a\mu_b}{(2\pi\hbar^2)^2}\ \frac{k_b}{k_a}\ \frac{\sum\limits_{M_AM_Bm_am_b} |T|^2}{(2J_A+1)(2J_B+1)} \tag{2.4}$$

The mu's are the reduced masses and the k's are the momenta. The transition amplitude, T, may be written

$$T = \int d\vec{r}_a \int d\vec{r}_b\ X_b^{-*}\ (\vec{k}_b\vec{r}_b) \langle bB|V|Aa\rangle X_a^{+}(\vec{k}_a\vec{r}_a) \tag{2.5}$$

where <bB|V|Aa> acts as an effective interaction producing the transition between the elastic states. The separation vectors $\vec{r}_a$ ($\vec{r}_b$) are the relative coordinates of particles a and A (b and B).

The transition amplitude may also be written in terms of reduced amplitudes, $\beta_{sj}^{\ell m m_a m_b}$

$$T = \sum_{\ell s j} \hat{j} \langle J_A|M_A, M_B-M_A|J_BM_B\rangle \beta_{sj}^{\ell m_b m_a} \tag{2.6}$$

where

$$\beta_{sj}^{\ell m m_b m_a} = i^{-\ell} \hat{j}^{-1} \sum_{m_a' m_b' m'} \langle \ell s m', m_a'-m_b' \ |j m-m_b+m_a\rangle$$

$$\times \langle s_a s_b m_a'-m_b' \ |s m_a'-m_b'\rangle\ (-)^{s_b-m_b'}$$

$$\times \int d\vec{r}_a \int d\vec{r}_b\ X_{m_b'}^{(-)*}\ (\vec{k}_b\vec{r}_b)\ G_{\ell sj,m'}(\vec{r}_b,\vec{r}_a)$$

$$X_{m_a'm_a}^{+}\ (\vec{k}_a\vec{r}_a)$$

and

$$\hat{j} = \sqrt{2j+1} \quad . \tag{2.7}$$

$G_{\ell sj,m}(\vec{r}_b,\vec{r}_a)$ is the radial form factor and contains all information about the radial part of the interaction. The $X^{+}_{m'm}$ $(X^{-*}_{m'm})$ are the distorted waves for the incoming (outgoing) particle. Part of the dependence of the distorted waves is on the projection quantum numbers of the projectile as a result of the $L \cdot S$ force in the optical potential. This dependence allows spin flip, polarization and asymmetry to be predicted in the absence of any spin dependent terms in the form factor.

The integral in equation 2.7 is over six dimensions and is time consuming to evaluate. To simplify this integral $\vec{r}_a$ and $\vec{r}_b$ may be taken to be parallel. This is obtained by assuming that particle b emerges from the location at which particle a is adsorbed. Algebraically this condition is $\vec{r}_b = (M_A / M_B)\,\vec{r}_a$. This is the zero range approximation. In this approximation, the parity change in the reaction is just $(-)^{\ell}$ where ℓ is the transferred orbital angular momentum. Particle exchange may be included in an approximate manner in the zero range approximation (PE 69), (PE 71).

2.4 Methods of Calculating the Spin Flip, Polarization and Asymmetry in the DWA

There are two viewpoints from which spin dependent quantities may be calculated. The first requires the development of a density matrix, ρ, for the interaction. With the density matrix, formulae may be developed for the polarization and spin flip. A detailed description of angular correlations calculated in the density matrix formalism is found in reference (RY 70). The second method divides the cross section into $(2s_a+1) \times (2s_b+1)$ partial cross sections $\sigma_{m_a m_b}$, where m_a and m_b are the particle spin projections taken with respect to a Z-axis perpendicular to the scattering plane, i.e., Z is along $\vec{k}_a \times \vec{k}_b$. For spin 1/2 particles, the spin flip, asymmetry and polarization are simple sums of these partial cross sections. These two approaches can be shown to reduce to one another.

Since the $\sigma_{m_a m_b}$'s can in principle be separately measured, it is appealing to the experimentalist to use them to calculate the other quantities. The defining formulae for $s_a = s_b = 1/2$ are

$$\sigma = \sigma_{++} + \sigma_{--} + \sigma_{+-} + \sigma_{-+}$$

$$\sigma A = \sigma_{++} + \sigma_{+-} - \sigma_{-+} - \sigma_{--}$$

$$\sigma P = \sigma_{++} - \sigma_{+-} + \sigma_{-+} - \sigma_{--}$$

$$\sigma S = \sigma_{+-} + \sigma_{-+} \tag{2.8}$$

If the Z-axis of quantization is taken perpendicular to the scattering plane (in the direction $\vec{k}_a \times \vec{k}_b$), these partial cross sections may be calculated by performing the sum over M_A and M_B in equation 2.4 while keeping the projectile spin projections distinct. Most formulations of the DWA algebra choose the Z-axis to be along the direction of the incident projectile momentum, $\vec{k}_a$. This choice greatly simplifies the algebra used in calculating the reduced amplitudes. However, the reduced amplitudes calculated in the coordinate frame with Z along $\vec{k}_a$ may be rotated into the coordinate frame with the Z axis along $\vec{k}_a \times \vec{k}_b$. The $\sigma_{m_a m_b}$'s may then be calculated directly. The form of this rotation is (SA 64)

$$\beta_{sj}^{\ell m m_b m_a}(a_1) = \Sigma\, \beta_{sj}^{\ell m' m_b' m_a'}(a_2)$$

$$\mathcal{D}^{j^*}_{\mu'\mu}(R_{21})\, \mathcal{D}^{s_b}_{m_b' m_b}(R_{21})\, \mathcal{D}^{s_a}_{m_a' m_a}(R_{21}) \tag{2.9}$$

where $\mu = m + m_a - m_b$ and R_{21} represents the set of Euler angles (BR 68) necessary to rotate coordinates a_2 into coincidence with coordinates a_1. The $\mathcal{D}^{j}_{\mu'\mu}(R)$ are the usual rotation matrices. The set of Euler angles $(\alpha, \beta, \gamma) = R_{21}$, which perform the rotation of Z along $\vec{k}_a$ to Z along $\vec{k}_a \times \vec{k}_b$, is $R_{21} = (-\pi/2, -\pi/2, 0)$. The code DWMAIN has been modified to calculate the rotated reduced transition amplitudes. From these, the partial cross sections, polarization, asymmetry, and spin flip are all obtained.

2.5 The Collective Model

The interaction potential for the collective model is derived from considering a deformation of the spherical nuclear potential well. The spherical potential well chosen is the one which gives the correct elastic scattering, i.e., the optical potential. A complete treatment of the deformation of the full optical potential, including the spin orbit term, has been done by H. Sherif (SH 67). His treatment is outlined here.

The T matrix for scattering from a 0^+ ground state to some state of spin J, parity $(-)^J$ is

$$T = \sum_{m_a m_b} \langle \chi^-_{m_b' m_b} (\vec{k}_a \vec{r}_a) | \langle JM\ 1/2\ m_b' | \Delta U | 00\ 1/2\ m_a' \rangle$$

$$| \chi^+_{m_a m_a} (\vec{k}_a \vec{r}_a) \rangle \tag{2.10}$$

where ΔU is the first order deformation of the optical potential. It is conventional to write this as a sum of the terms in the optical potential

$$\Delta U = \Delta U_C + \Delta U_R + \Delta U_i + \Delta U_{so} \tag{2.11}$$

The central parts of ΔU are obtained by expanding the radial parameters in the density function $f(r, R, a)$ so that $R \rightarrow R + \alpha(\hat{r})$, and $f(r, R + \alpha, a) = f(r, R, a) + \alpha(\hat{r}) \frac{\partial f}{\partial r}$ where $\hat{r}$ is the angular coordinates. The central terms of the optical potential become

$$\Delta U_r + \Delta U_i = -\alpha(\hat{r}) \Big(V_R \frac{\partial}{\partial R_R} f(r, R_R, a_R)$$

$$+ (W_V - 4a_i W_{SF} \frac{\partial}{\partial r}) \frac{\partial}{\partial R_I} f(r, R_I, a_I)\Big) \tag{2.12}$$

where the deformation of the real and imaginary parts is assumed to be the same. To derive ΔU_{so}, consider U_{so} written in explicit form

$$U_{so} = \left(\frac{\hbar}{m_\pi c}\right)^2 (V_{so} + iW_{so})\ \sigma\cdot(\vec{\nabla}\rho(\vec{r}) + \frac{1}{i}\vec{\nabla}) \tag{2.13}$$

where $\rho(\vec{r})$ is the nuclear matter density distribution and both a real and imaginary potential strength are considered. If $\rho(\vec{r})$ is represented by the density function $f(r, R_{so}, a_{so})$ and the first order expansion is made, ΔU_{so} becomes

$$\Delta U_{so} = \left(\frac{\hbar}{m_\pi c}\right)^2 (V_{so} + iW_{so})\ \vec{\sigma}\cdot[\vec{\nabla}(\alpha_{so}(\hat{r})\frac{\partial f}{\partial R_{so}}) \times \frac{1}{i}\vec{\nabla}] \tag{2.14}$$

Performing the gradient on $\alpha_{so}(\hat{r})\frac{\partial f}{\partial R_{so}}$ we may write $\Delta U_{so} = \Delta U_{so}^{(1)} + U_{so}^{(2)}$, where

$$\Delta U_{so}^{(1)} = \left(\frac{\hbar}{m_\pi c}\right)^2 (V_{so} + iW_{so})\ \alpha_{so}(\hat{r})\ \frac{1}{r}\ \frac{\partial}{\partial r}\ \frac{\partial f}{\partial R_{so}}\ \vec{\sigma}\cdot\vec{\ell} \tag{2.15}$$

and

$$\Delta U_{so}^{(2)} = \left(\frac{\hbar}{m_\pi c}\right)^2 (V_{so} + iW_{so})\ \frac{\partial f}{\partial R_{so}}\ \vec{\sigma}\cdot[\vec{\nabla}(\alpha_{so}(\hat{r}) \times \frac{1}{i}\vec{\nabla}]$$

The sum $\Delta U_{so}^{(1)} + \Delta U_{so}^{(2)}$ is called the full Thomas form of the deformation. Using the usual multipole expansion $\alpha(\vec{r}) = \sum_{\ell m} a_{\ell m}\, Y_\ell^{*m}(\hat{r})$ the matrix element of $\alpha(\hat{r})$ is given by

$$\langle JM|\alpha(\hat{r})|00\rangle = \frac{\beta_J R}{\sqrt{2J+1}}\ Y_J^{*m}(\hat{r}) \tag{2.16}$$

where β_J is the deformation parameter. The interaction matrix for the central part, including Coulomb excitation, is then just

$$\begin{aligned}\langle JM|\Delta U_{cent}|00\rangle &= \frac{\beta_J}{(2J+1)^{1/2}} [V_o R_R \frac{\partial f}{\partial R_R} \\ &\quad - i\, R_I (W_V - 4a_I W_{SF} \frac{\partial}{\partial r}) \frac{\partial f}{\partial R} \\ &\quad + \frac{3Zze^2}{R_c(2J+1)} \times \begin{matrix} (r/R_c)^J & r<R_c \\ (R_c/r)^J & r\geq R_c \end{matrix}] Y_J^{*M} (\hat{r}) \\ &= i^J G_{JOJ}(r) Y_J^{*M}(\hat{r}) \qquad (2.17)\end{aligned}$$

which is factored into a radial form factor and an angular part (see equation 2.7). The matrix elements for ΔU_{so} are

$$\begin{aligned}\langle JM|\Delta U_{so}^{(1)}|00\rangle &= \frac{\beta_J^{so}}{\sqrt{2J+1}} (\frac{\hbar}{m_\pi c})^2 R_{so} [V_{so} + iW_{so}] \\ &\quad \times \frac{1}{r} \frac{\partial^2 f}{\partial r\, R_{so}} \; Y_J^{M^*} (\hat{r}) \vec{\sigma}\cdot\vec{\ell} \qquad (2.18)\end{aligned}$$

and

$$\begin{aligned}\langle JM|\Delta U_{so}^{(2)}|00\rangle &= \frac{\beta_J^{so}}{(2J+1)^{1/2}} (\frac{\hbar}{m_\pi c})^2 R_{so} [V_{so} + iW_{so}] \\ &\quad \frac{\partial\, f}{\partial R_{so}} \vec{\sigma}\cdot(\vec{\nabla}(Y_J^{M^*}(\hat{r})) \times \frac{1}{i} \vec{\nabla}) \\ &\qquad (2.19)\end{aligned}$$

Since $\langle JM|\Delta U_{so}^{(2)}|00\rangle$ contains an operator which differentiates the distorted waves, it is not simply calculated in the "standard" codes, such as JULIE, DWMAIN or DWUCK. These codes calculate the radial form factor and distorted waves separately. The overlap integral is then numerically preformed on the product of the incoming and outgoing distorted waved and the form factor. H. Sherif has written a DWA code (SH 68) which includes the full Thomas form of the distorted spin-orbit potential.

The terms which include the derivatives of the distorted waves are included. The deformation parameters β_J and β_J^{so} are left as free parameters so that the relative deformation strength may be varied.

2.6 The Microscopic Model

The matrix element $\langle bB|V|Aa\rangle$ in equation 2.5 may be calculated using nuclear wave functions which are a superposition of the wave functions of the individual nucleons in the initial and final states. The interaction potential V operates between single nucleon initial and final states. These two nucleon matrix elements, weighted and summed, comprise a microscopic discription of the scattering reaction.

In the zero range approximation, using an interaction potential which ignores the L·S force, the form factor $G_{\ell sj,m}$ of equation 2.7 may be factored and calculated separately. In order to separate the radial and angular dependence of the interaction potential, it may be written in a multipole expansion (SA66)

$$V(\vec{r}, \vec{x}_a, \vec{x}_A) = \sum_{LSJ,\mu} (-)^{J-\mu} V_{LSJ,\mu}(r, \vec{x}_A) \\ T_{LSJ-\mu} (\hat{r}, \vec{x}_a) \qquad (2.20)$$

where

$$T_{LSJ-\mu} = \sum_m \langle LSm, \mu-m|J\mu\rangle i^L \; Y_\ell^m(\hat{r}) \; S_{s\mu-m} (\vec{x}_a)$$

is the spin-angle tensor. By defining (PE 71) the transition density

$$F^{LSJ}(r_o) = \sqrt{2} \langle J_B || \sum_i \frac{\delta(r_o - r_i)}{r_o^2} T^{LSJ}(i) || J_A \rangle \tag{2.21}$$

the radial form factor, $G_{LSJ}(r)$, becomes

$$G_{LSJ}(r) = \int v_{LS}(r, r_o) F^{LSJ}(r_o) r_o^2 dr_o \quad . \tag{2.22}$$

The multipole coefficients v_{LS} are the coefficients of the multipole expansion of the potential.

One potential used here is the Kallio - Kolltveit (KK) (KA 64) interaction. This potential is written

$$V^{TE} = 475 \exp(-2.5214 (r - 0.4))$$

$$V^{SE} = 330 \exp(-2.4021 (r - 0.4)) \tag{2.23}$$

for $r > 0.4$ and

$$V^{TE} = V^{SE} = \infty$$

for $r \leq 0.4$, where TE and SE refer to the triplet and singlet parts of the interaction in total spin which have even symmetry in the spatial coordinates.

Another potential which may be used has the Yukawa form

$$V(r) = V \frac{e^{-\alpha r}}{\alpha r}$$

In comparison to the KK potential, if a 1 fermi range is used for the Yukawa potential, then the strengths of $V(r) = V_0(r) + V_1(r)\, \vec{\sigma}_1 \cdot \vec{\sigma}_2$

	V_0	V_1	(MeV)
pp	-18.4	18.4	
pn	-54.0	-5.75	(2.24)

will produce equivalent results (PE 71).

The nuclear wave functions used to calculate the transition density were those of D. M. Clement and E. Baranger (CB) (CL 68). These wave functions were calculated in a space of twelve single particle orbits for both protons and neutrons. The quasi-particle Hamiltonian was diagonalized between the excited states J^π formed by a superposition of two neutron quasi-particles coupled to J^π and proton particle-hole excitations coupled to J^π and a closed core ground state. The transition density is (CO 70)

$$F^{LSJ}(r) = \sum_{jj'} Z_{jj'} \left(U_j V_{j'} + (-)^{L+S} U_{j'} V_j\right)$$

$$\Psi_{jj'} \left(1 + \delta_{jj'}\right)^{-1/2} \tag{2.25}$$

with

$$Z_{jj'} = \frac{1}{\sqrt{\pi}}\ \hat{j}'\hat{\ell}\hat{\ell}'\hat{L}\hat{S}\hat{J}\ (-)^{\ell} \begin{pmatrix} \ell' & L & \ell \\ 0 & 0 & 0 \end{pmatrix} \begin{Bmatrix} \ell' & 1/2 & j' \\ L & S & J \\ \ell & 1/2 & j \end{Bmatrix}$$

$$u_{n\ell}(r)\ u_{n'\ell'}(r) \tag{2.26}$$

where U_j and V_j are the occupation parameters (BA 60), $\Psi_{jj'}$ is the amplitude from Clement and Baranger, and $u_{n\ell}$ is the radial part of the nuclear wave function calculated in an harmonic oscillator potential well.

The FORTRAN codes FBART and NUCFAC (PE 70) were used to calculate the transition density and form factor for input to DWMAIN. Values of $\Psi_{jj'}$ and V_j used in these calculations are in Table 2.1

Table 2.1 Clement and Baranger Wave Functions and Occupation Numbers for ^{120}Sn and ^{124}Sn 2^+ States

neutrons		^{120}Sn		^{124}Sn	
j	j'	$\Psi_{jj'}$	V_j	$\Psi_{jj'}$	V_j
p3/2	p3/2	-.013	.99634	-.01	.99683
	p1/2	-.023		-.02	
	f5/2	-.011		-.01	
	f7/2	.046		.04	
p1/2	f5/2	-.024	.99503	-.02	.99563
f5/2	f5/2	-.019	.99565	-.02	.99612
	h9/2	.139		.14	
	f7/2	-.001		.00	
g9/2	g9/2	.040	.99416	.04	.99523
	d5/2	.081		.06	
	g7/2	.037		.03	
	i13/2	-.144		-.13	
d5/2	d5/2	.080	.97475	.06	.98314
	g7/2	.045		.03	
	s1/2	.187		.12	
	d3/2	.132		.09	
g7/2	g7/2	.155	.95506	.11	.97140
	d3/2	.309		.21	
s1/2	d3/2	.321	.89252	.22	.94295
d3/2	d3/2	.299	.69423	.24	.82497
h11/2	h11/2	-.602	.50763	-.74	.67294
	h9/2	-.074		-.11	
h11/2	f7/2	-.170		-.20	
h9/2	h9/2	-.092	.18520	-.13	.23899
h9/2	f7/2	.015		.02	
i13/2	i13/2	.058	.10566	.06	.11668
f7/2	f7/2	-.040	.11569	-.04	.13197

protons		^{120}Sn	^{124}Sn
j	j'	$\Psi_{jj'}$	$\Psi_{jj'}$
p3/2	f7/2	-.063	-.06
f7/2	h9/2	-.155	-.16
f5/2	f7/2	.005	.01
g9/2	d5/2	.311	.28
g9/2	g7/2	.108	.10
g9/2	i13/2	-.164	-.16

3. EXPERIMENTAL PROCEDURE

3.1 Cyclotron and Experimental System

Proton beams for this experiment were accelerated by the Michigan State University sector focused cyclotron (BL 66). Normally 100% of the internal H^+ beam was extracted via an electrostatic deflector and magnetic channel. Figure 3.1 shows the floor plan of the cyclotron experimental area and beam line used.

The beam transport system (MA 67) focused the extracted proton beam from the cyclotron on slits S1. After being bent through 90° by magnets M3 and M4, a second focus was formed at slits S3. Beam divergence was limited by slits S2. Typical slit openings for this experiment were .100 inches for all slits. These slit values limit the FWHM energy spread to 8 parts in 10^4.

Proton energies were determined from nuclear magnetic flux meters in the central fields of M3 and M4. The energy of the analyzed beam as a function of magnetic field strength has been calculated (SN 66). Recent measurements based on a new technique (TR 70) have allowed the calibration of the absolute energy of the analyzed beam to better than 1 part in 1000.

The analyzed beam was deflected into the target chamber by magnet M5, and focused at the target center. No collimating slits are used between M5 and the faraday cup in order to minimize radiation background in the experimental

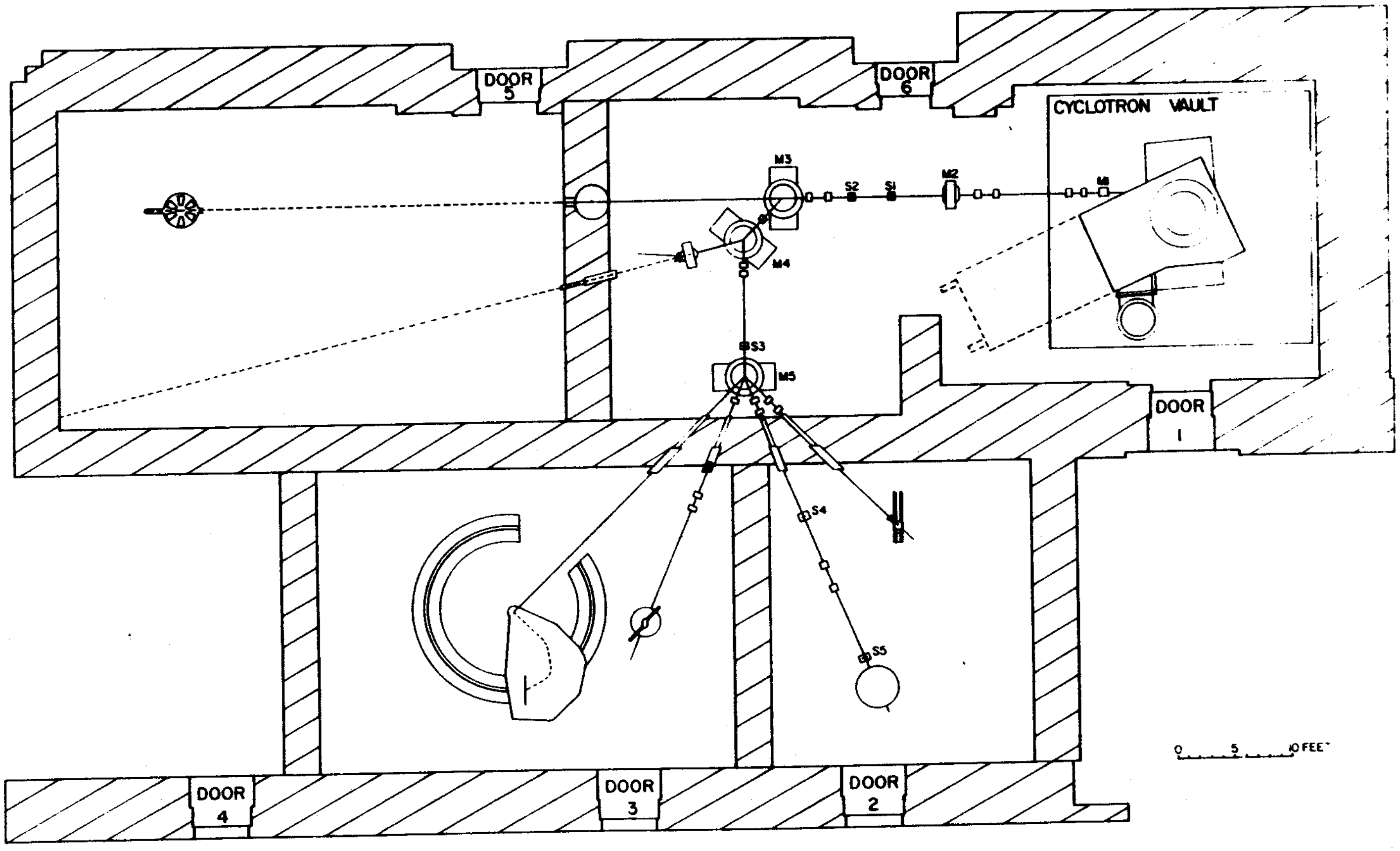

Figure 3.1 Experimental area of the Michigan State University Cyclotron Laboratory.

area. The focused beam was typically rectangular, 1 mm high and 3 mm wide. The beam was positioned by observing the beam spot relative to fiducial marks inscribed on a one half mm thick piece of plastic scintillator viewed with a closed circuit television system. This allowed positioning of the beam spot to within 20 mils.

Targets for this experiment were isotopically enriched self-supporting rolled foils of ^{120}Sn 9.9 mg/cm^2, 98.4% isotopic purity and ^{124}Sn 5.13 mg/cm^2, 94.7% isotopic purity. The isotopes were obtained from the Isotopes Division of Oak Ridge National Laboratory and the targets fabricated at Microfoils Inc., Argonne, Illinois. Since target thickness and uniformity are unimportant in the reduction of the data, thickness was determined by weighing only.

The targets were mounted in the existing target chamber (KO 69) which allows remote positioning of both target height and angle.

Beam exiting the target chamber was collected in a 2.9 inch diameter by 59 inch long faraday cup. The beam stop was located 2 m beyond the target position. With this distance, radiation from the faraday cup reaches the gamma detector approximately midway in time between radiation counts from other beam bursts at the target.

The beam stop was a .75 inch carbon block chosen for its low neutron production characteristics. The whole faraday cup was encased in a 22 inch diameter by 34 inch long cylindrical water shield to further reduce the neutron flux.

The beam current and integrated charge were measured with an Elcor Model A 310 B current integrator connected to the faraday cup.

3.2 Detectors

Gamma rays were detected in this experiment with a Harshaw Integral Line 2 inch diameter by 3 inch long NaI(Tl) crystal coupled to a RCA 8575 photo multiplier tube. This detector has a measured energy resolution of 7.6% for the 662 KeV gamma ray from ^{137}Cs.

Bias voltage was supplied to the photo multiplier by an ORTEC 265 photo tube base. This base is designed so that the photo tube anode is maintained at ground potential, thus the anode signal rise time is not limited by the time constant derived from a large coupling capacitance.

The ORTEC 265 base allows external voltage stabilization of the final four photo tube dynodes. Current flow from the voltage divider resistance chain through the dynodes during pulse amplification increases the total current in the resister chain. This increases the potential between the first few dynodes and the photo cathode. The effect of this is a rather strong gain increase with increasing count rates. This effect may be reduced by adding large capacitors in parallel with the resistors in the voltage divider chain. Since the fraction of the capacitors' charge necessary to compensate for the lost dynode electrons is small, these serve to hold the interdynode voltage difference more constant. Expanding on this technique, batteries or Zener diodes may be used to supply the voltage to the dynodes. In practice, Zener diodes and .5 μf capacitors were placed in parallel with the last four dynodes. The zener diodes were chosen such that the interdynode voltages were those supplied by the base with an overall operating voltage of -3000 V. The operating voltage used was -1800 V. This increased the relative amplification of the last four, stablized, dynodes in comparison to the normal amplification at -1800 V. In this configuration, the shift of the centroid of the 1.33 MeV gamma line from ^{60}Co was 5% (compared to 100% without stabilization) when the counting rate was varied from 100/sec to 65,000/sec.

To reduce background, the gamma detector was encased in a lead cylinder with 4 inch thick walls and 24 inches long. The shielding weight was 1/2 ton and was moved along a line centered to within 10 mils of target center by a motorized screw jack. The measured total displacement off center is 10 mils. With this shield, the background from sources other than the target was measured to be 10% of the total counting rate when using a tin target.

The product of the gamma-ray detector efficiency and solid angle was determined directly in the experimental apparatus. A ^{60}Co radioactive source calibrated to ±2% at the MSU Cyclotron Lab (KO 69) of known activity was placed at the position of the center of the target. Observation of the 1.17 MeV gamma-ray from this decay provided the detector efficiency-solid angle product, $\varepsilon\Delta\Omega$, for the 1.17 MeV gamma-rays. Only the photo peak in the gamma-ray spectrum is used in calculating $\varepsilon\Delta\Omega$. The efficiency-solid angle for 1.13 MeV gamma-rays was obtained from this with a small correction (HE 64). The efficiency-solid angle product for the gamma-ray photo peak and the face of the gamma-ray detector at 6 1/8 inches from the source was determined to ±6% accuracy to be 1.16×10^{-3} steradian for 1.17 MeV (^{120}Sn) and 1.24×10^{-3} steradian for 1.13 MeV (^{124}Sn).

To detect charged particles a 5 mm x 500 mm^2 lithium drifted silicon detector was used. A detector of large surface area was necessary in order to obtain a sufficiently large proton solid angle.

To provide a suitable environment for operating the detector outside of the target chamber, a portable vacuum box was constructed (see Figure 3.2). Protons entered the box through a 1 mil aluminum window. Solid angle definition was obtained with collimators placed in a holder in front of the particle window and external to the vacuum. The detector was housed in the box in a brass

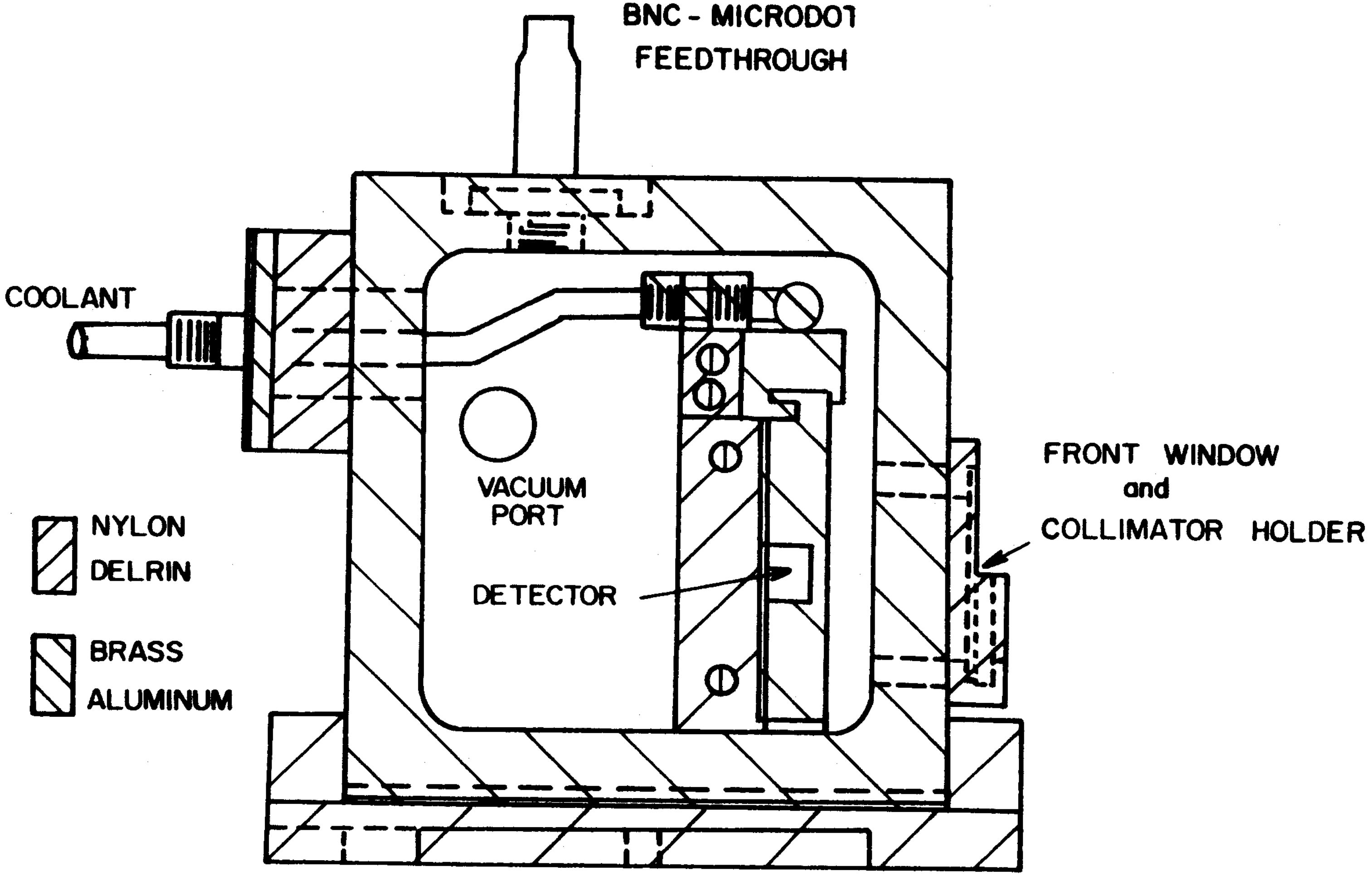

Figure 3.2 Side view of vacuum box housing the particle detector.

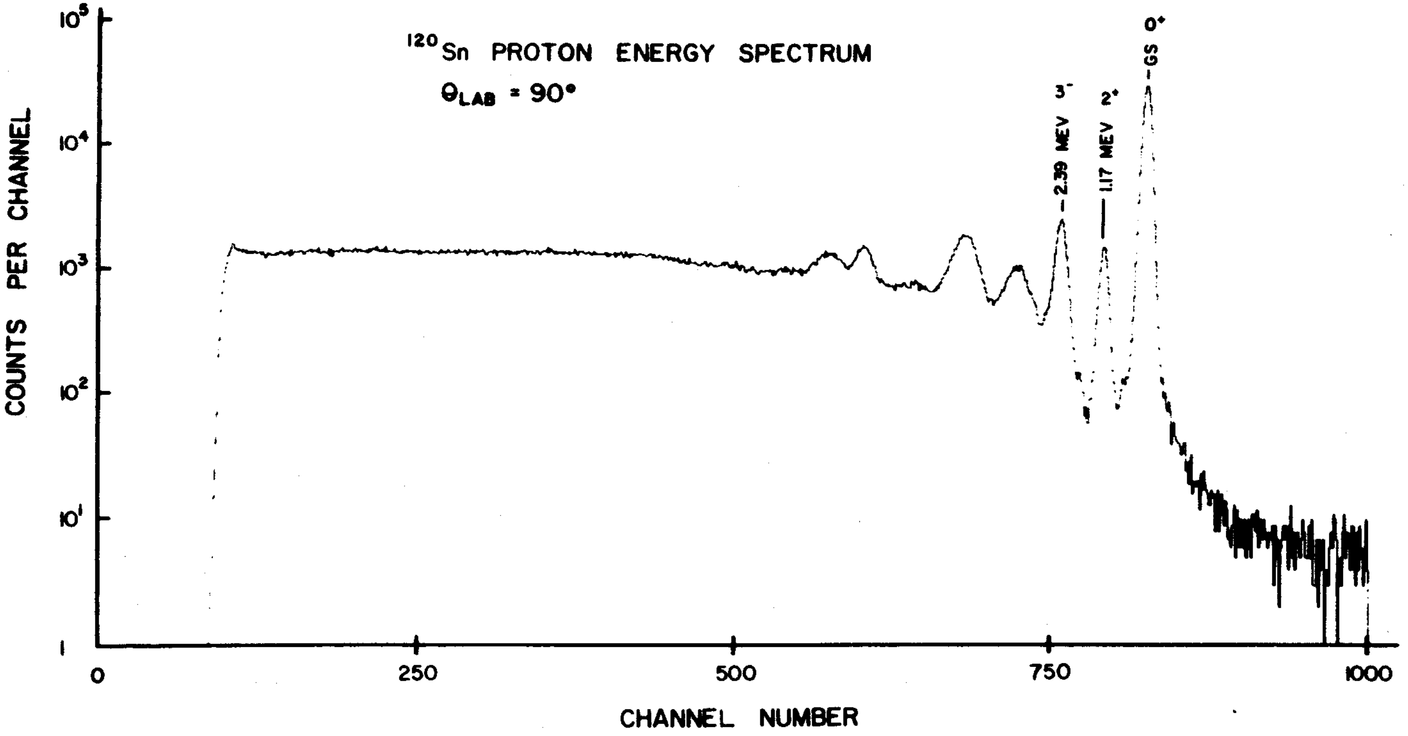

Figure 3.3 Typical proton pulse height spectrum.

holder to which alcohol cooled by dry ice was pumped from an external source. The detector holder was fastened to the wall of the vacuum box with Delrin plastic mounts which provided both heat and electrical insulation for the detector and mount. After a period of rough pumping vacuum was maintained with a cryogenic pump filled with molecular sieve and kept at liquid nitrogen temperatures.

A typical spectrum of protons scattered from ^{120}Sn and detected with this system is shown in Figure 3.3. The resolution for the elastically scattered protons is 250 KeV FWHM.

3.3 Electronics

Because the coincidence count rate is limited mainly by the limit on the count rate in the gamma-ray channel, the electronics were designed to extend this limit to as high a count rate as possible. In particular, dead time and pile up effects must be minimized. To reduce electronic dead times, cable delays and cable delays with amplifiers were used instead of gate and delay generators on all timing and logic signals in the gamma channel. Also, 100 nsec differentiation and integration constants were used to shape the bipolar gamma pulse.

A block diagram of the electronics configuration appears in Figure 3.4. Fast timing signals from a timing single channel amplifier (TSCA) set on the bipolar proton amplified pulses started the time to amplitude converter

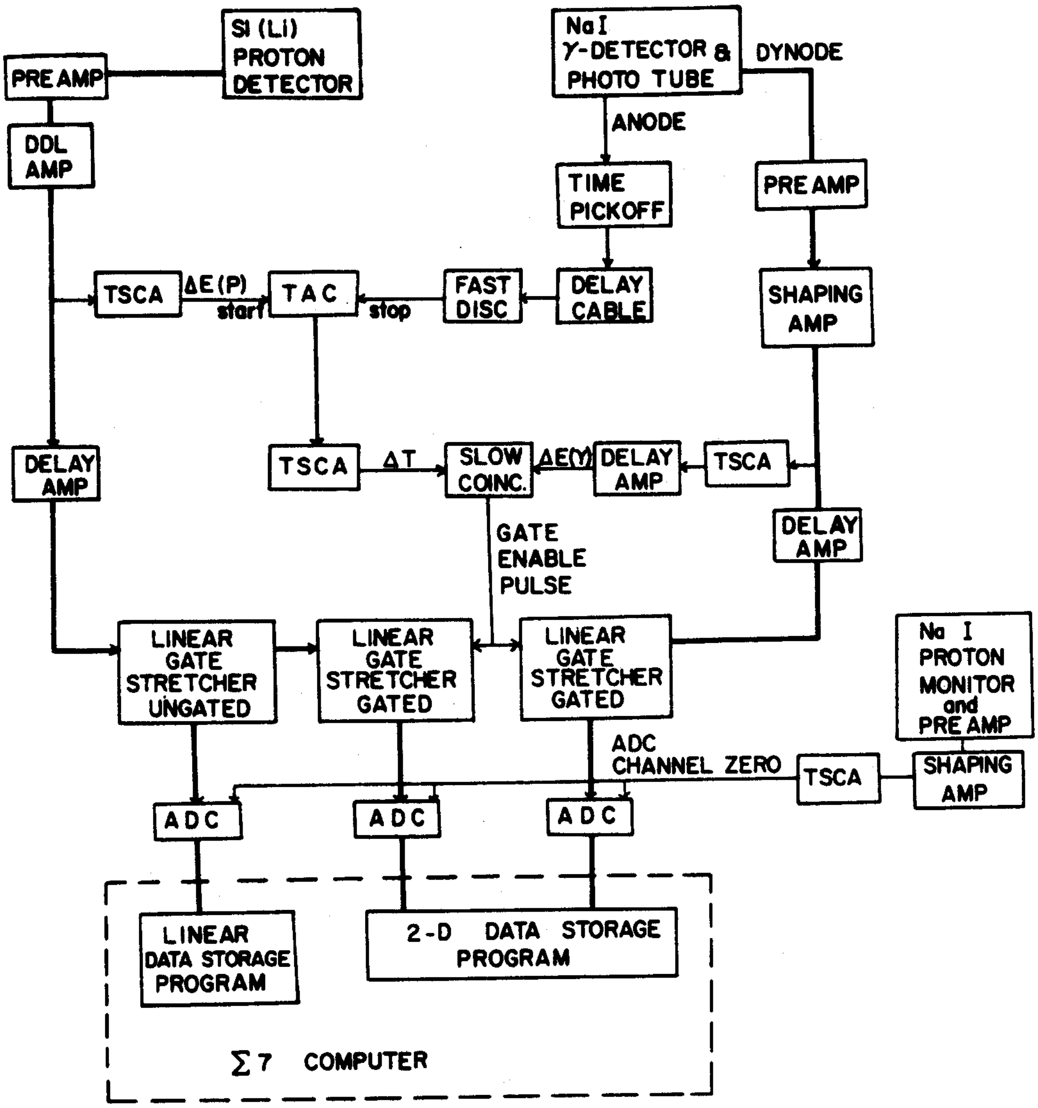

Figure 3.4 Block diagram of the electronic system.

(TAC). Although the TSCA cross-over timing pulses were quite pulse-height dependent, the high efficiency and simplicity in use of cross-over timing over other timing methods were judged more important than improved time resolution in this case. Delayed signals from an inductive pick up coupled to the anode of the gamma detector photo tube were used to stop the TAC. A typical time spectrum is shown in Figure 3.5. TAC starts were selected from protons scattered from states of 0 to 3 MeV excitation in the tin target. The spectrum passed through a linear gate enabled by a TSCA which selected pulses between 0.7 and 1.5 MeV in the gamma-ray energy spectrum.

The large peaks are due to the pulsed nature of the cyclotron beam which has a period of 61.5 nsec at 30 MeV. Structure within these peaks was observed to correspond to TAC starts from protons scattering from separate energy levels in the tin nucleus. This was done by observing the time spectra of each proton state in relationship to the cyclotron rf. This structure is due to charge collection effects in the silicon detector integrated into the double-delay-line amplified proton pulse. These charge collection effects are seen in doped germanium and silicon detectors where the mobility of electrons and holes are different. The shape of the detector output has two slopes on the leading edge of the output pulse resulting from the separate carrier mobilities. This difference in mobility results in a difference in the

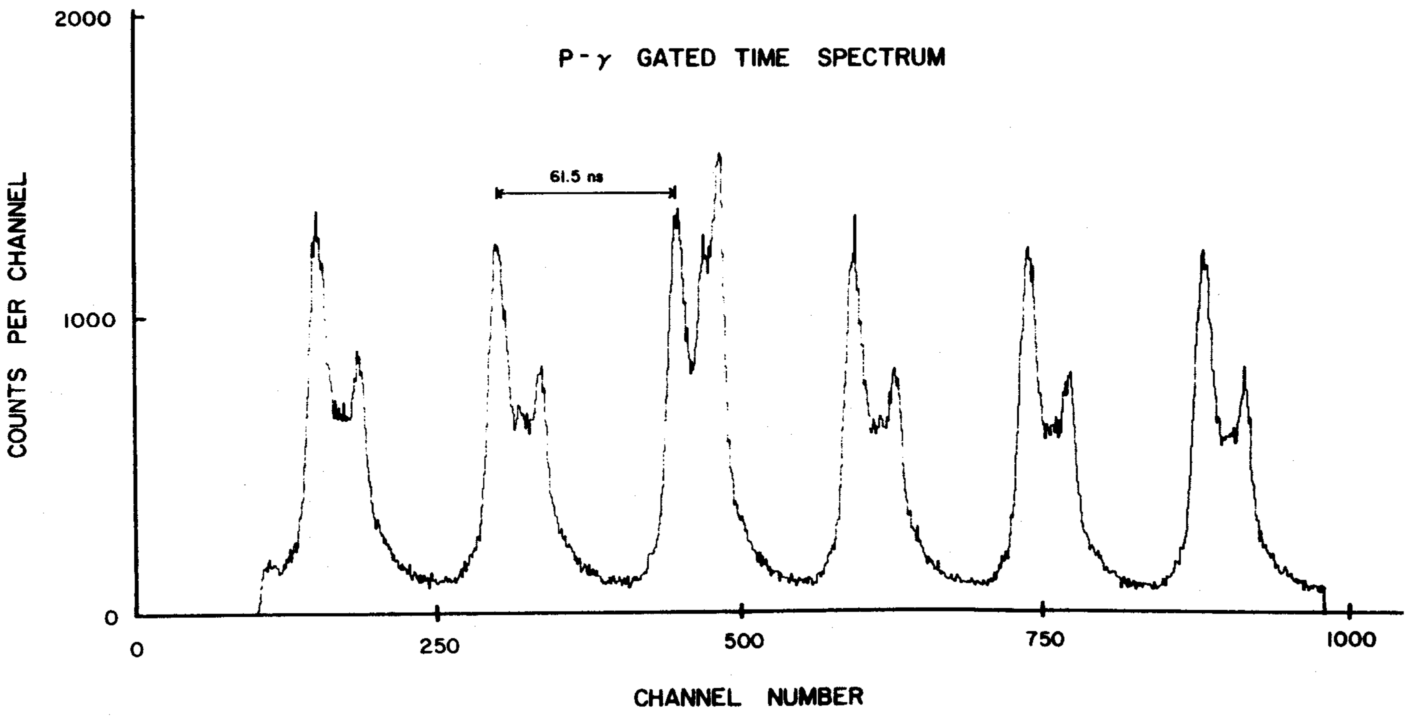

Figure 3.5 Typical TAC output pulse height spectrum.

shape of the leading edge of the pulse obtained from events in various parts of the detector. Pulses from protons of different energies and thus different ranges in the silicon detector have different pulse shapes. In cross-over timing these differences appear as changes in the time output relative to the initial pulse.

Other fast timing techniques such as timing derived from an inductive pickup leading edge timing coupled to the unamplified proton pulse eliminated the structure in the peaks in the time spectrum. However, in this method the electronics available at the MSU Cyclotron Laboratory did not generate timing signals with 100% efficiency. Because of the slow rise time (the specified charge collection time for the detector is 500 nsec) of the detector output, the inductive coupling did not produce pulses sufficiently large to reliably trigger the unit's timing discriminator.

The peak containing true coincidence events is identified by an increase in the starts from excited states (the right half of the peaks) while elastic events contribute equally to all peaks. The full width at half maximum of the total peak is 22 nsec.

Events from the true coincidence peak were selected by a TSCA set on the output of the TAC. A slow coincidence was required between the output of the TSCA set on the fast time spectrum and the output of the TSCA set on the gamma-ray energy spectrum. The output of the slow coincidence unit was used to enable a pair of linear gate stretchers (LGS). The LGS's passed pairs of coincident proton and gamma-ray pulses for pulse height analysis. These pulses were converted by two ADC's and stored in the set up (2-D) mode in a 128 x 128-channel array by the program TOOTSIE (BA 69). The conversion gain and digital offsets of the ADC's were varied so that the proton and gamma-ray pulse height ranges selected by the respective TSCA's filled the center region of the array. An example of such an array is seen in Figure 3.6.

Pulses converted by one ADC without a coincident pulse being converted by the second ADC are stored along the axes of the 2-D display. The counts on the axis in this experiment represent cases in which the corresponding coincident pulse was rejected by the LGS. This can occur if the internal discriminator of the LGS is triggered by a prior pulse and has not yet reset at the arrival of the gate enable signal (OR 69). The method for handling these counts is described in the data reduction section.

The 2-D array was displayed on an oscilloscope and markers were set to extract gamma-ray energy spectra corresponding to coincidences with protons of chosen energy bins.

Ungated, stretched proton pulses were analyzed by a third ADC and after conversion were stored in a 1024-channel spectrum using the data-taking program POLYPHEMUS (AU 69). Collection of this singles spectrum for the

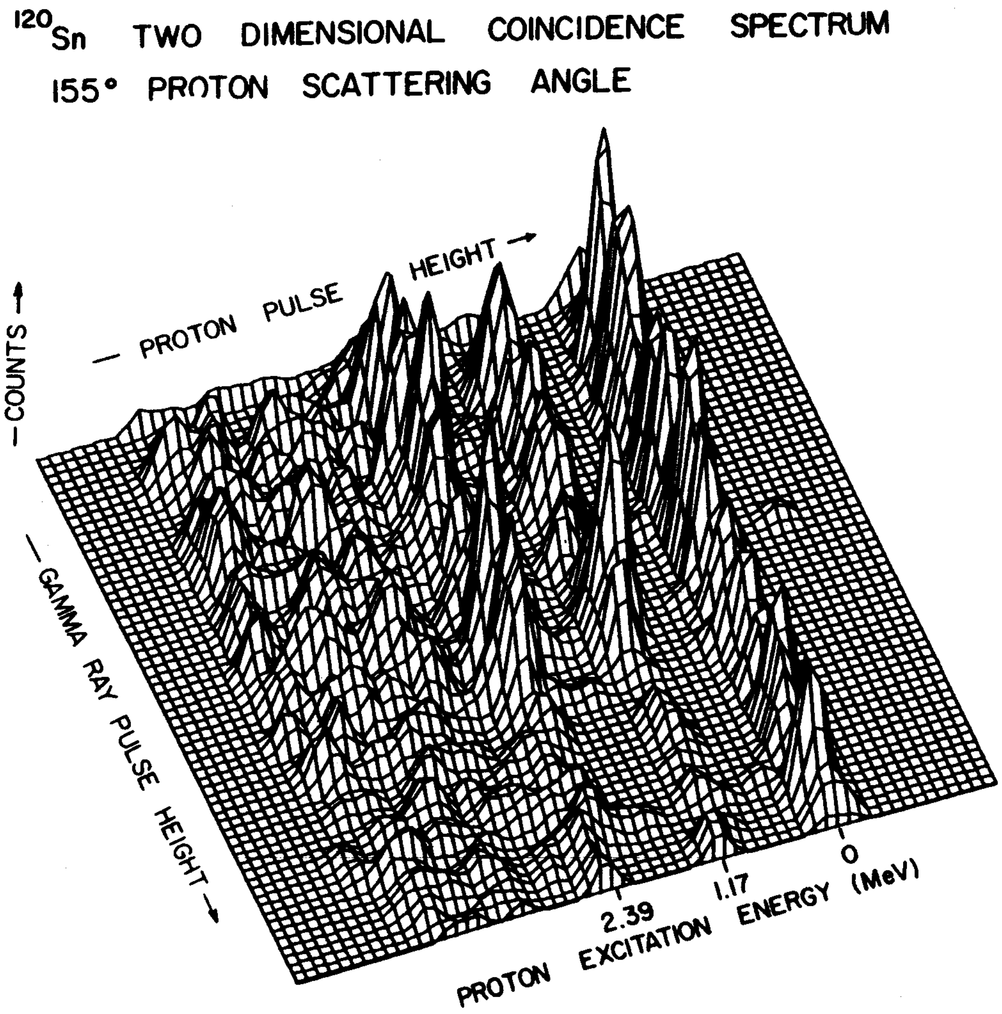

Figure 3.6 Two parameter coincidence data

whole run at each angle provided a convenient normalization for the coincidence data. Collection of the singles spectrum in this manner eliminates charge collection, target thickness and target uniformity as parameters in reduction of the coincidence data.

A monitor counter served to measure the dead time of the ADC's. A selected portion of the monitor spectrum was counted on a scaler and in channel zero of the ADC's. This was typically about 3% for the proton singles counts and always less than .1% for the case of the coincidence counts. Also, proton starts, gated gamma-ray stops, true coincidence gate-enables and all elastic events in the monitor were separately counted on scalers in order to monitor the course of the experiment and to calculate dead-time corrections. The selected one dimensional coincidence spectra, the 2-D coincidence array and the singles proton spectrum were stored on cards for later analysis.

Figure 3.7 shows a typical set of one dimensional coincidence gamma-ray spectra for one run along with a singles gamma-ray spectrum and a "standard" line shape. The one dimensional gamma-ray spectra were taken for proton energy bins which encluded the whole proton peak. The peak seen in the second excited state spectrum was always easily observed and results from the two nearly equal energy gamma-rays (1.22 MeV 3^- to 2^+ and 1.17 MeV 2^+ to 0^+) produced by the cascade of the strongly excited 3^- state decaying through the first excited 2^+ state to the ground

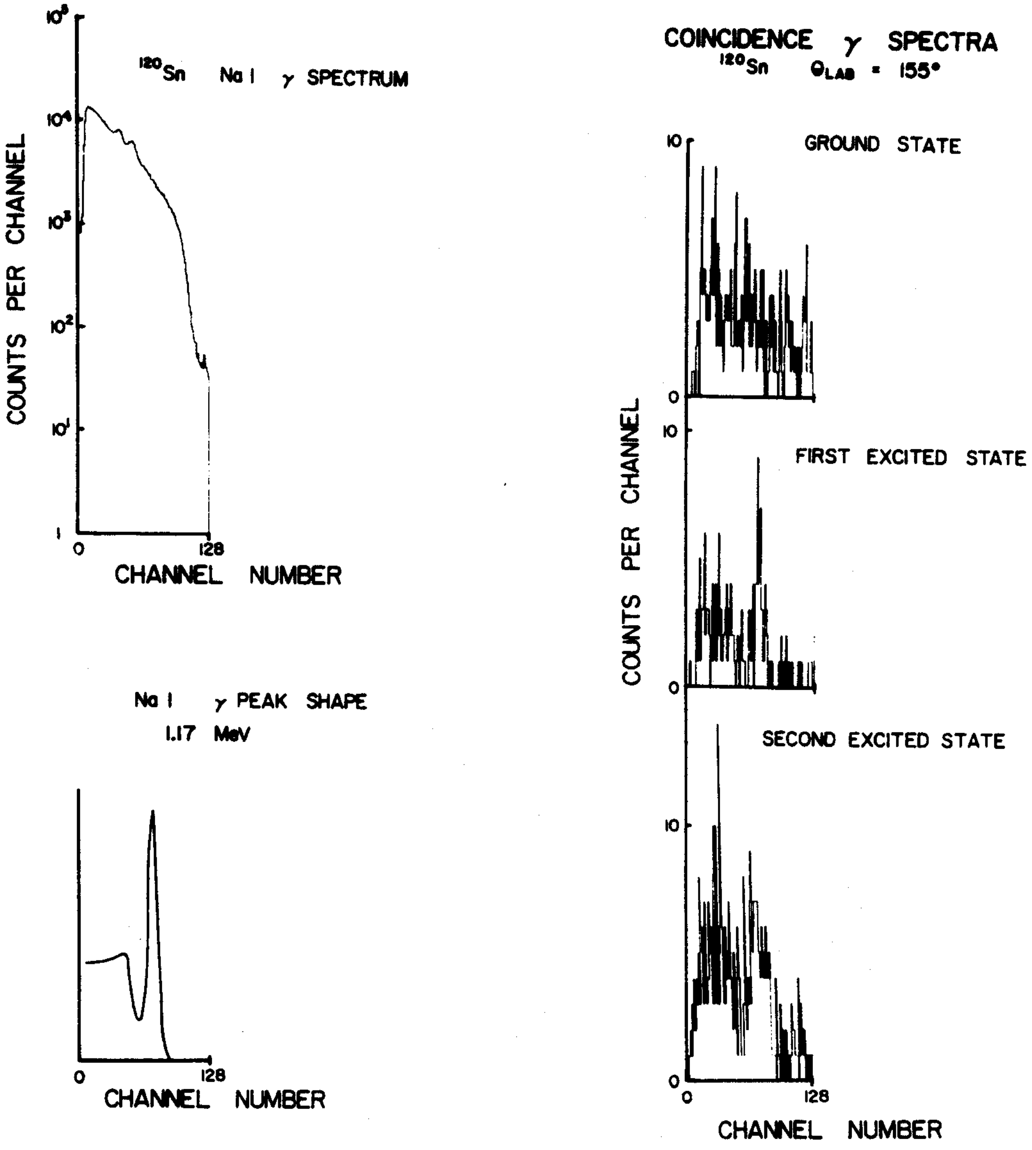

Figure 3.7 Gamma-ray singles and coincidence spectra with standard line shape.

state. In ^{124}Sn these two gamma-rays were not as close in energy (1.42 MeV 3^- to 2^+ and 1.13 MeV 2^+ to 0^+) and could be separately observed. For both nuclei, collection of the second excited state coincidences served as an added calibration which was quite useful when the number of real coincidences in the first excited state was small. The peaks in the singles spectrum contain not only the gamma-rays from the de-excitation of ^{120}Sn but also gamma-rays resulting from the β-decay of Sb^{118} to $^{118}\mathrm{Sn}^*$. ^{118}Sb is obtained through the (p, 3n) reactions on ^{120}Sn.

3.4 Data Reduction

The probability for a proton scattered through some angle θ to have its spin flipped is, for infinitesimal detector apertures,

$$S(\theta) = \frac{8\pi}{5} \frac{1}{(\varepsilon d\Omega)_\gamma} \frac{R}{N} , \qquad (3.1)$$

where θ is the proton scattering angle $(\varepsilon d\Omega)_\gamma$ is the solid angle-efficiency product of the gamma-ray detector, N is the total number of inelastic scattering events to the 2^+ state and R is the number of real proton-gamma-ray coincidences.

The number of real coincidences, R, was determined for a proton pulse height bin, $\Delta E_p\ 2^+$, which enclosed the 2^+ proton peak and a gamma ray bin, $E_\gamma PP$, which enclosed only the photo peak of the $2^+ \rightarrow 0^+$ gamma ray. So R is

$$R = \sum_{\substack{\Delta Ep(2^{+}\ \text{state}) \\ \Delta E\ (2^{+} \rightarrow 0^{+}\ \text{photo peak})}} R(E\gamma,\ Ep) = R(\ E\gamma PP,\ \Delta Ep\ 2^{+}) \qquad (3.2)$$

The number of real coincidences R(Eγ, Ep) as a function of gamma ray and proton pulse height (Eγ and Ep) is determined from the total number of measured coincidences, T(Eγ, Ep), at the same Eγ and Ep. In any coincidence system with finite time resolution, random, accidental coincidences may occur. These accidental counts A(Eγ, Ep) were determined and subtracted from T(Eγ, Ep) to obtain R(Eγ, Ep). In calculating real counts as a function of Eγ and Ep it is convenient to sum T(Eγ, Ep) over some pulse height bin ΔEp(ΔEγ) and calculate R(Eγ, ΔEp) (R(ΔEγ, Ep)) as a function of only the gamma ray (proton) pulse height.

A spectrum of accidental counts was determined as a function of Eγ for some proton bin ΔEp. A real counts spectrum, R(Eγ, ΔEp), was then obtained from the equation

$$R(E\gamma,\ \Delta Ep) = T(E\gamma,\ \Delta Ep) - A(E\gamma,\ \Delta Ep)\ . \qquad (3.3)$$

This equation is also valid for ΔEγ, Ep sets.

Uncorrelated spectra, i.e., spectra which contain no real coincidences, or for which no coincidence requirement was imposed, may be used to calculate A(Eγ, ΔEp). A(Eγ, ΔEp) (A(ΔEγ, Ep)) will be proportional, within statistics, to any random coincidence spectrum U(Eγ, ΔEp') (U(ΔEγ', Ep)) which is the same function of Eγ(Ep) but calculated for any $\Delta Ep'(\Delta E\gamma')$. This is also true for the singles spectra $U(E\gamma$, singles) and $U(Ep$, singles). Thus,

$$A(E, \Delta E) = K\, U(E, \Delta E') \qquad (3.4)$$

for either $E\gamma$, $\Delta Ep'$ or Ep, $\Delta E\gamma'$.

The proportionality constant K is obtained from a second U. For example, if $U(E\gamma, \Delta Ep$ g.s.) = $T(E\gamma, \Delta Ep$ g.s.) were taken from random gamma-ray-proton ground state coincidences and $A(E\gamma, \Delta Ep\ 2^+)$ were desired to calculate $R(E\gamma, \Delta Ep\ 2^+)$ with equation 3.3, K could be calculated from the proton singles spectrum. In this case, K is just the ratio of counts in $U(Ep$, proton singles), $K = \frac{U(\Delta Ep\ 2^+,\ \text{proton singles})}{U(\Delta Ep\ \text{g.s.},\ \text{proton singles})}$. In addition to $U(E\gamma, \Delta Ep$ g.s.) and $U(Ep$, proton singles) an uncorrelated spectrum may be obtained by choosing $\Delta E\gamma$ to include only pulse heights greater than the value Ex possible from a decay of some proton excitation at Ep, i.e., $U(\Delta E\gamma > Ex, Ep) = T(\Delta E\gamma > Ex, Ep)$.

In practice, the calculation of $R(E\gamma, \Delta Ep\ 2^+)$ as described in the above example, was used to obtain R. $R(\Delta E\gamma$ P.P., Ep) was also calculated to check the limits of ΔEp for the 2^+ state. A computer program was written which allowed input of either the one dimensional coincidence spectra or the 2-D coincidence array in order to calculate the real coincidence gamma-ray spectra for the first and second excited states. A second, similar program calculated real coincidence proton spectra.

The photo-peak was often distinguishable in the real coincidence gamma-ray spectrum for the first excited state, R(Eγ, ΔEp 2^+). When this was obtained, a bin of gamma-ray pulse heights was chosen to include only the photo-peak. The number of real counts in this bin was used to calculate the spin flip (see equation 3.1). In cases where the number of real coincidences for the 2^+ state was small, the real coincidence spectrum containing the cascade gamma-rays ($3^- \rightarrow 2^+$, $2^+ \rightarrow 0^+$) of the strongly excited 3^- (^{120}Sn 2.39 MeV and ^{124}Sn 2.55 MeV) state was heavily relied upon to define the limits of an acceptable gamma-ray bin. The photo-peak of the 2^+ to 0^+ member of the cascade decay was always clearly distinguishable in R(Eγ, ΔEp 3^-). This peak has the same gamma-ray energy and thus pulse height as the ($2^+ \rightarrow 0^+$) decay obtained by directly exciting the 2^+ state. Since this peak is sensitive to all the same experimental conditions, such as gain shifts, as the peak expected in the real coincidence spectrum for the first excited state, the limits obtained from inspecting this peak could be directly applied to the real coincidence spectrum for the directly excited 2^+ state.

Real counts along the Ep axis were scaled and added to those in the gamma-ray energy bin. It is presumed that these counts represent a random sampling of the counts throughout the gamma-ray energy spectrum. Thus real counts along the axis were scaled by the ratio of the number of real counts in the selected gamma-ray energy bin to the total number of real counts. Addition of the real events along the proton axis typically lead to an increase in the total number of real events of 5% and never more than 15%.

The statistical standard error, $\delta S(\theta)$, associated with $S(\theta)$ (equation 3.1) is

$$[\delta S(\theta)]^2 = [\frac{8\pi}{5}\frac{1}{(\epsilon d\Omega)_\gamma}]^2 [T(2^+) + K^2U + U^2(\delta K)^2] / N \quad , \qquad (3.5)$$

where the pulse height summations over ΔEp and $\Delta E\gamma$ in T and U are implicit and the error in N is small and omitted from this formula.

The formula for $S(\theta)$ in terms of R/N when detectors subtend finite solid angles is not as simple as formula 3.1. The radiation pattern for gamma-rays resulting from a spin-flip ($\Delta m = \pm 1$) transition is peaked along the line perpendicular to the scattering plane. Also the radiation patterns for the non-spin-flip ($\Delta m = 0, \pm 2$) transitions are not zero near the perpendicular (SH 70). Thus, to calculate $S(\theta)$ for a finite gamma-ray detector and a point proton detector, one must take the weighted average of the spin-flip gamma-ray radiation pattern over the detector solid angle and subtract the contribution of real coincidences from non-spin-flip transitions. The number of real coincidences in a finite gamma-ray detector which can result from non-spin-flip transitions is a function of the relative populations of the m = 0 and m = ±2 (non-spin-flip) sublevels of the excited 2^+ state. Each has a separate distribution in de-excitation.

The position of a particle detector with infinitesimal aperture defines the scattering plane. An aperture of finite size will define an envelope of scattering planes. Each scattering plane in the envelope is weighted by the fraction of the total accepted particle flux contributed from that plane. The size of the envelope depends on the scattering angle, becoming larger as the scattering angle changes from 90° in the laboratory.

In this experiment $S(\theta)$ was calculated with a formula (HI 70) which is a function of scattering angle, the ratio of the m = +2 to the m = 0 substate populations, the half angle acceptances of the proton and gamma detectors, the geometry of the proton detector aperture and the dependence of the gamma-ray detector efficiency on the angle of incidence of the gamma-ray. The derivation of this formula assumes that the gamma-ray detector is circular and that the m = +2 and m = -2 sublevels are populated equally. The formula is:

$$
\begin{aligned}
S(\theta) = {} & 2[1.6(1+2q)\,R/N - 3A_4B_1 - 6A_2B_2 + 2.25A_5B_3 \\
& + 18A_6B_4 + 6A_3B_5 + q(.75A_5B_3 - 2A_1 \\
& + 6A_6B_4 + 2A_3B_5)]/[2A_1 - 9A_4B_1 - 18A_2B_2 \\
& + 7.5A_5B_3 + 60A_6B_4 + 20A_3B_5 + q(7.5A_5B_3 \\
& - 6A_4B_1 - 12A_2B_2 + 60A_6B_4 + 20A_3B_5)]
\end{aligned}
\tag{3.6}
$$

where

$$A_1 = \int_0^{x_\gamma} \sin x\ p(x)dx \qquad B_1 = \int_0^{x_p} \frac{f(x)x^2dx}{\sin^2\theta\ +x^2}$$

$$A_2 = \int_0^{x_\gamma} \cos^2 x\ \sin\ p(x)dx \qquad B_2 = \int_0^{x_p} \frac{f(x)\sin^2\theta dx}{\sin^2\theta\ +x^2}$$

$$A_3 = \int_0^{x_\gamma} \cos^4 x\ \sin\ p(x)dx \qquad B_3 = \int_0^{x_p} \frac{f(x)x^4dx}{(\sin^2\theta+x^2)^2}$$

$$A_4 = \int_0^{x_\gamma} \sin^3 xp(x)dx \qquad B_4 = \int_0^{x_p} \frac{f(x)x^2\sin^2\theta dx}{(\sin^2\theta+x^2)^2}$$

$$A_5 = \int_0^{x_\gamma} \sin^5 xp(x)dx \qquad B_5 = \int_0^{x_p} \frac{f(x)\sin^4\theta dx}{(\sin^2\theta d+x^2)^2}$$

$$A_6 = \int_0^{x_\gamma} \cos^2 x\sin^3 xp(x)dx$$

and

$P(x)$ = the angular dependent gamma-ray detector efficiency

x_i = the half angle acceptance of the i^{th} detector

$f(x)dx$ = a weighting function defined by the shape of the proton detector aperture which gives the fraction of protons between angles x and x+dx

$q = a_2/a_0$ is the ratio of the population of the m=+2 nuclear substate to the m=0 substate.

Figures 3.8 and 3.9 show the spin flip angular distributions for ^{120}Sn and ^{124}Sn when calculated with formula 3.1 which assumes that both detector apertures are infinitesimal. Figures 3.10 and 3.11 show the same angular distributions when calculated with formula 3.6. In the later calculations

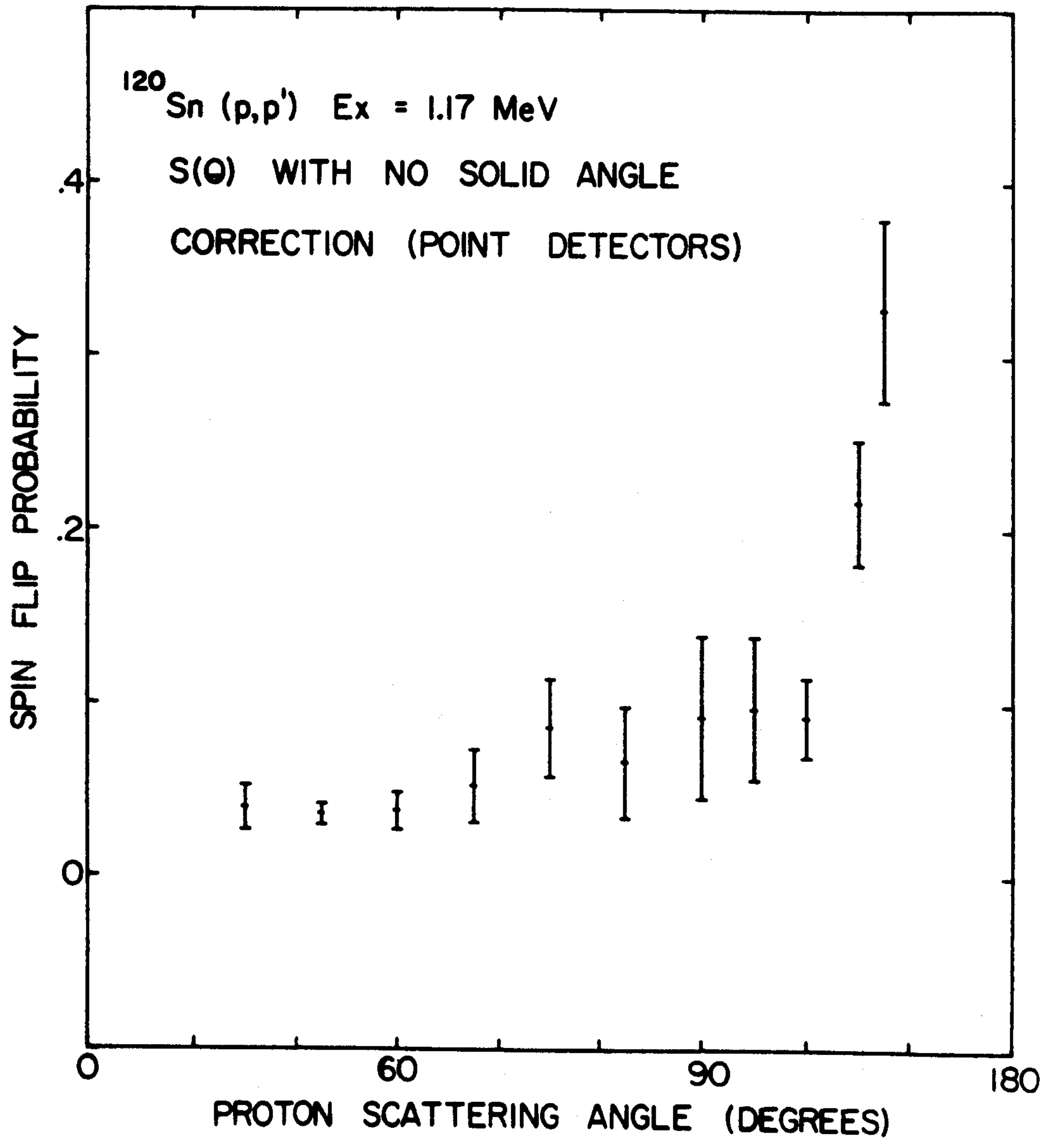

Figure 3.8 ^{120}Sn spin-flip data without detector solid angle corrections.

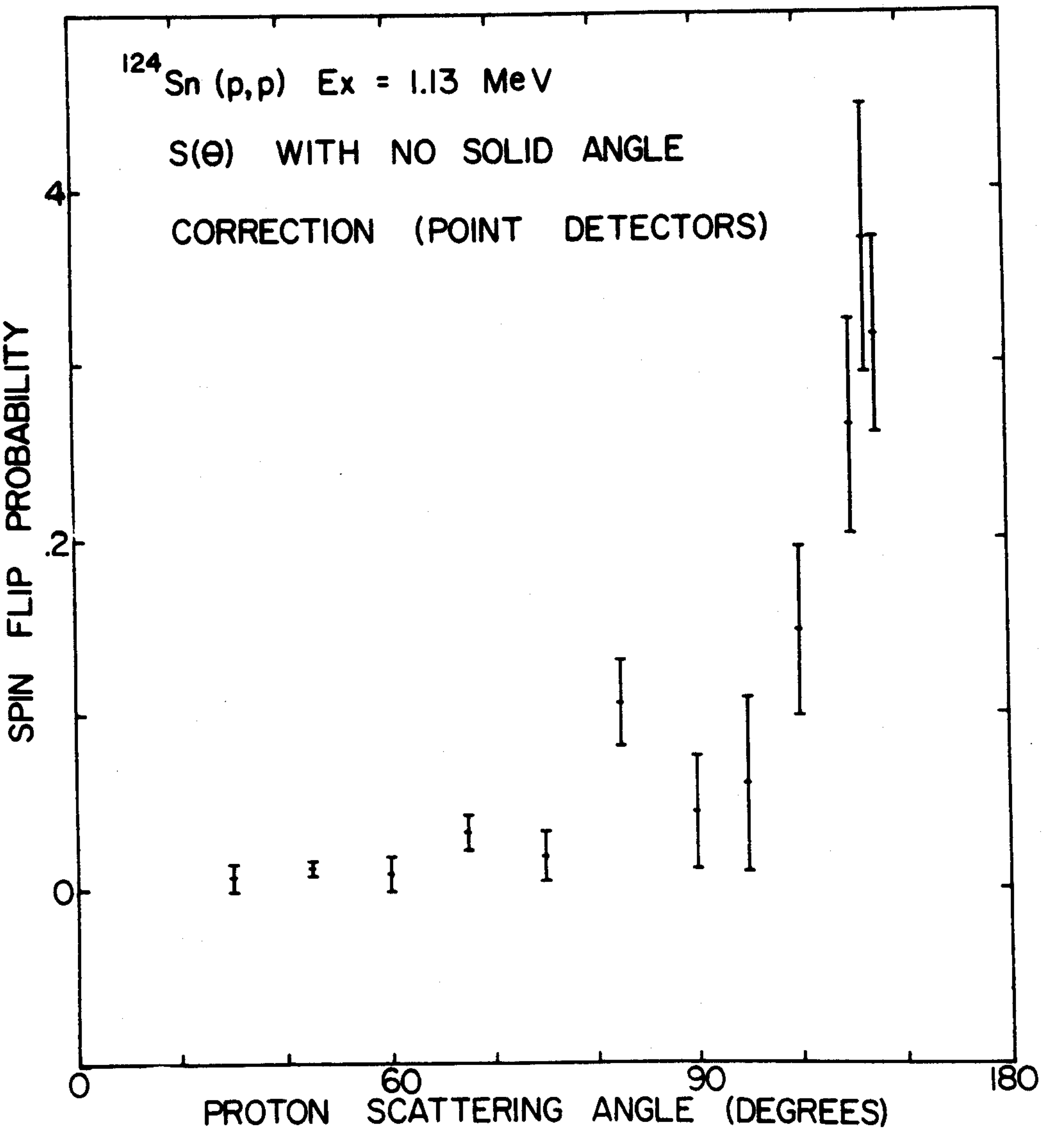

Figure 3.9 ^{124}Sn spin-flip data without detector solid angle corrections.

$$P(x) = (\epsilon d\Omega)_\gamma / d\Omega_\gamma = \text{constant},$$

$$f(x) = 4 / x_p \pi \sqrt{1 - (x / x_p)^2}$$

and

$$a_2 / a_0 = q = 1.$$

The half angular acceptances are $x_p = .07$ rad. and $x_\gamma = .134$ rad. The errors shown in Figures 3.8 and 3.9 are only statistical. In Figures 3.10 and 3.11, the errors include the RMS sum of the statistical error and an estimate of the error generated in choosing $q = 1.0$. In neither case was the ±6% normalization error resulting from the uncertainty in the gamma-ray detector efficiency included.

Since the actual substate populations are unknown and can be measured only with substantial effort, the values of $S(\theta)$ calculated at each angle with $q = 0$ and $q = \infty$ represent the limits of possible values of $S(\theta)$. The values of these limits with purely statistical errors are shown in Figures 3.12 and 3.13. Plus or minus one third the difference between these limiting values was used as an estimate of the uncertainty generated by the arbitrary choice of q. This contribution doubled the error on some forward angle data where the statistical error is small, but increased the error in the back angle data by about 10% of the statistical error.

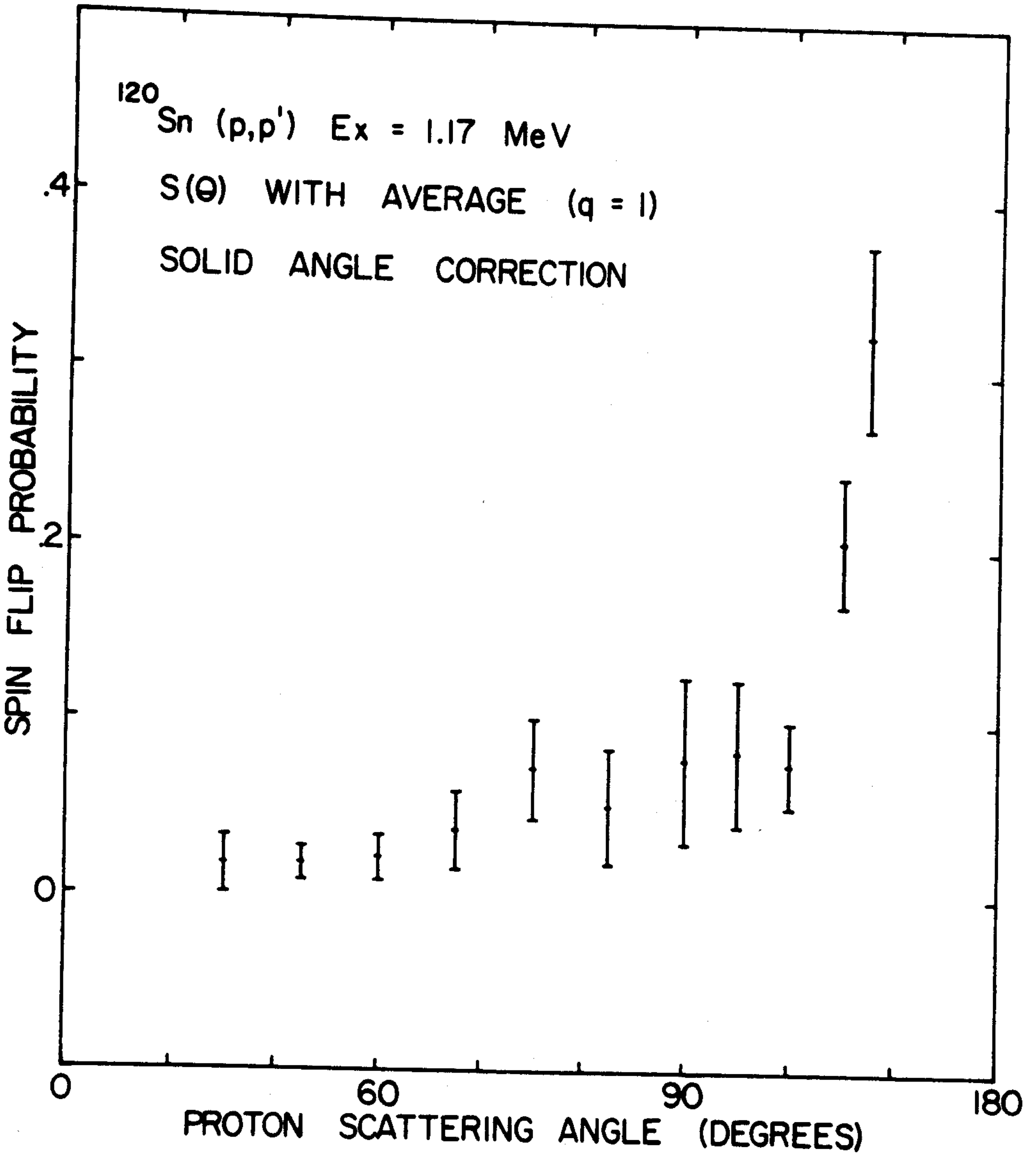

Figure 3.10 ^{120}Sn spin-flip data with an average solid angle correction (q = 1).

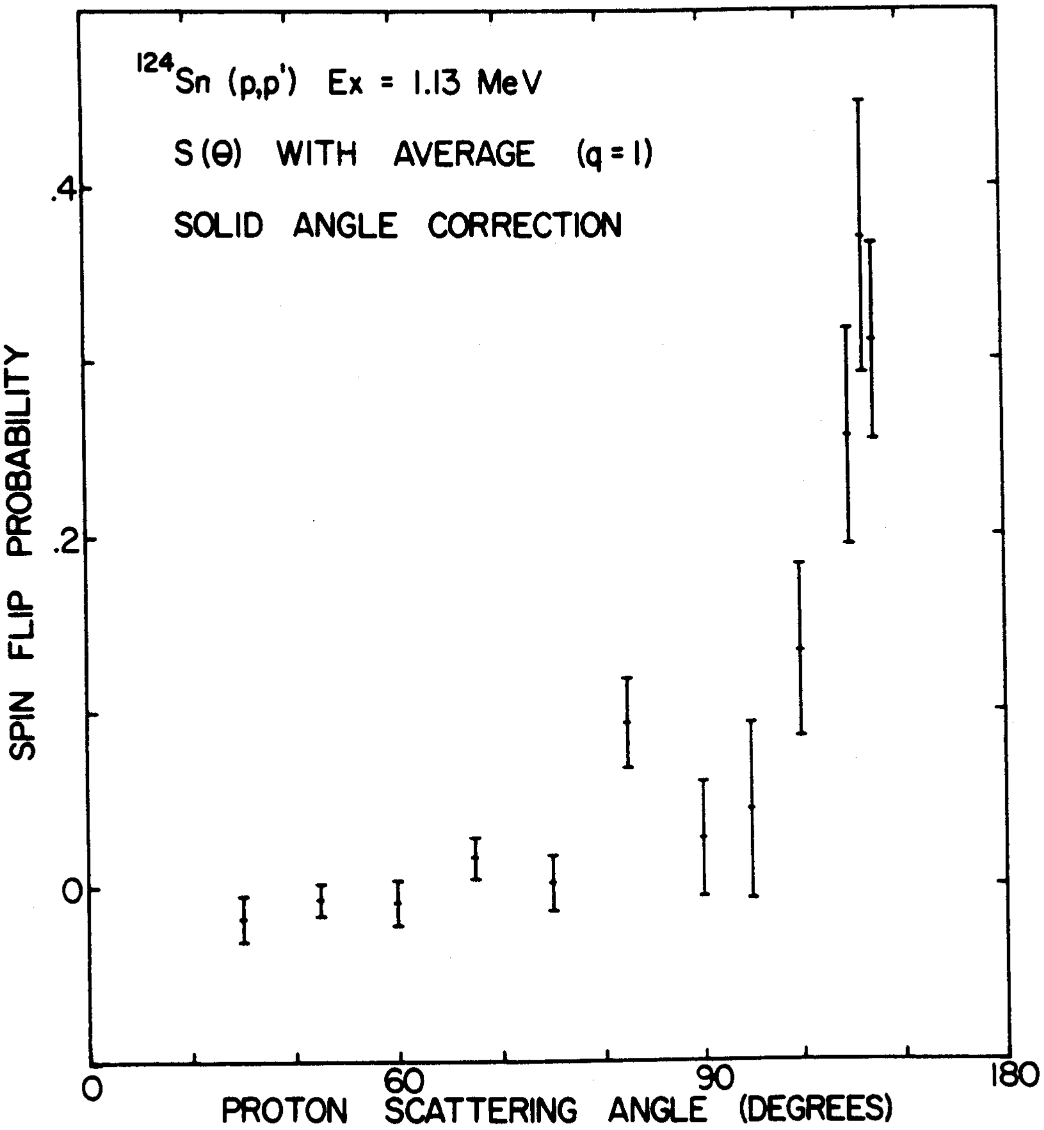

Figure 3.11 ^{124}Sn spin-flip data with an average solid angle correction (q = 1).

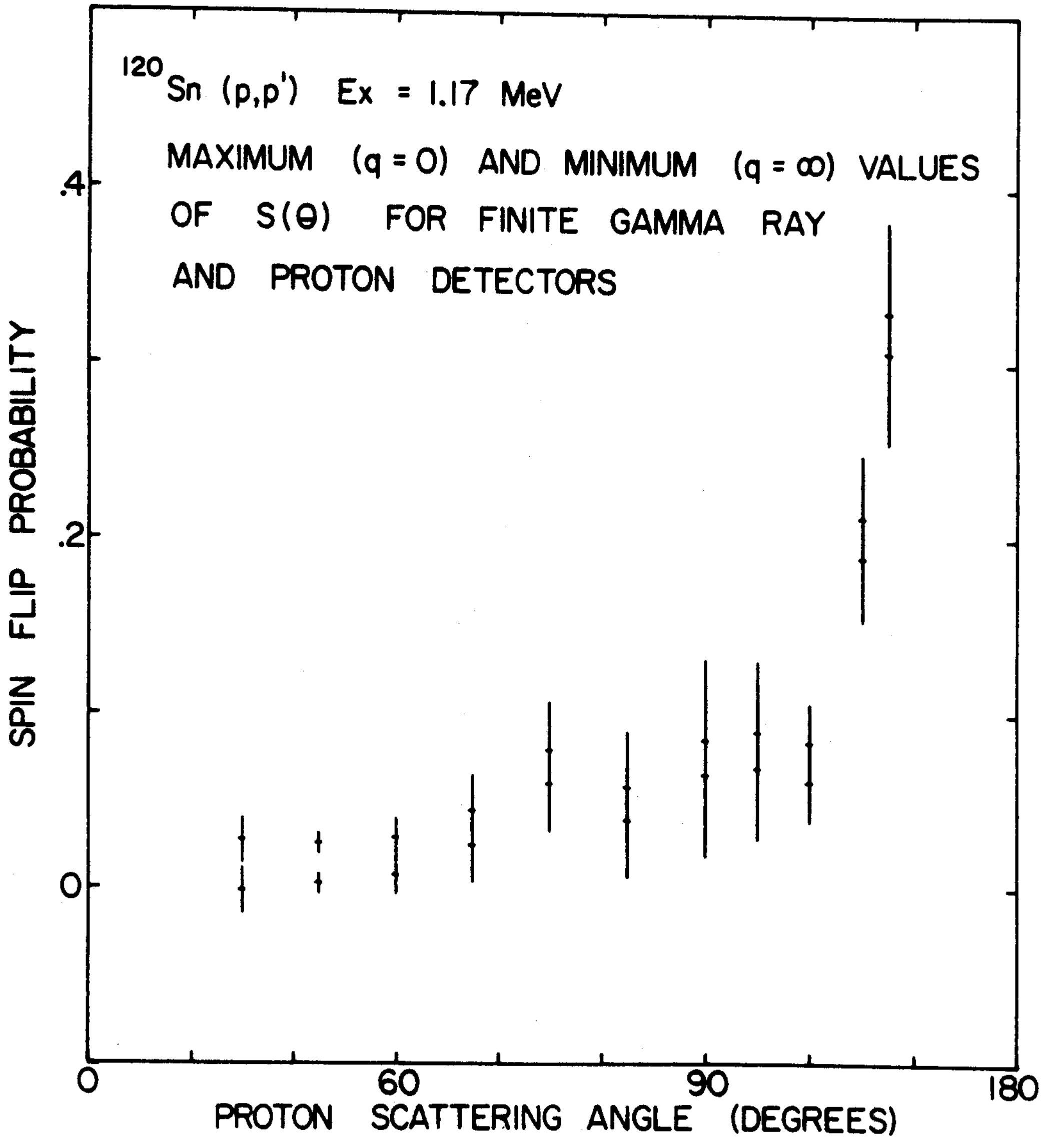

Figure 3.12 ^{120}Sn spin-flip data with maximum (q = ∞) and minimum (q = 0) solid angle corrections.

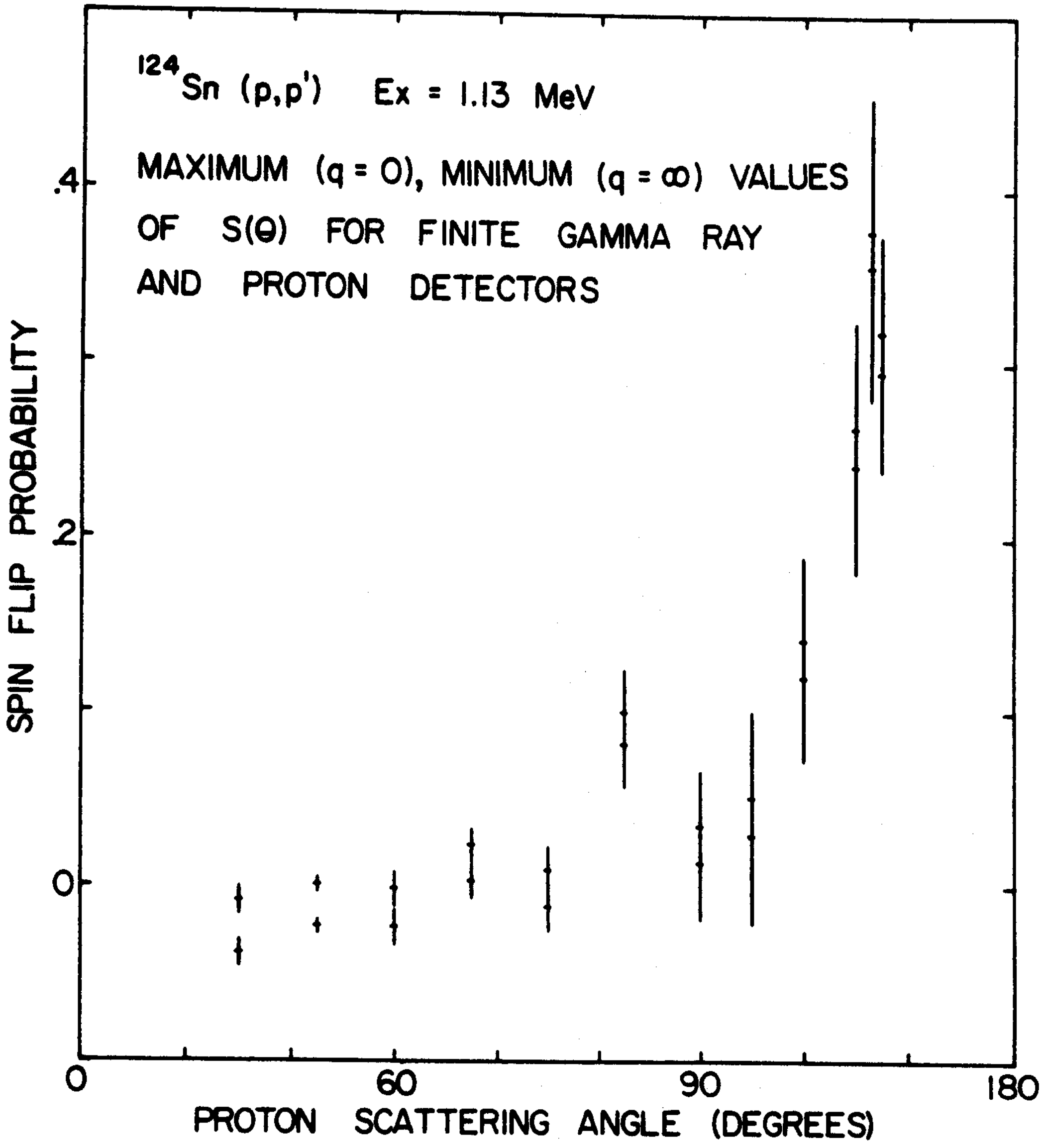

Figure 3.13 ^{124}Spin-flip data with maximum (q = ∞) and minimum (q = 0) solid angle corrections.

Calculating S(θ) with Formula 3.6 resulted in lower values than those obtained by assuming that the detectors had infinitesimal apertures. This is especially true for the forward angle ^{124}Sn data where the choice of any value of q greater than zero results in values of S(θ) (see Figure 3.13) which are negative outside the experimental error. The data on ^{120}Sn and ^{124}Sn are quite similar. The main difference between the two isotopes is seen at angles forward of 75° where the ^{120}Sn data is consistantly higher than that of ^{124}Sn.

4. DATA ANALYSIS

4.1 Inelastic Scattering Data

The spin flip data treated in this section represents many lengthy periods of data collection on the cyclotron. Data taken at forward angles represent the shortest data collection time, requiring about four hours per angle. At backward angles as long as twenty hours of data collection time was spent on one point. Because of the length of time invested in obtaining a data point at some angle and because of the regular nature of the data at forward angles, the angular distribution was taken at 15° intervals. The data sets considered in this section have been corrected for experimental solid angle effects as described in the experimental section of this work.

Elastic and inelastic cross-section data was obtained along with the spin flip data at each angle in the spin flip angular distribution. The large solid angle acceptance of the proton detector used in this experiment averages the cross-section measurement over its angular aperture and degrades the usefulness of the cross-section data.

Both inelastic cross-section and inelastic asymmetry data are available in the literature for protons at 30 MeV for ^{120}Sn (KA 70). These data are included in this analysis of proton scattering.

4.2 Elastic Scattering Data and Optical Model Parameters

The basic set of scattering data at 30 MeV, including elastic cross-sections, reaction cross-sections, and elastic polarizations on targets from C to Pb was taken at the Rutherford High Energy Lab (RHEL) (CR 64, RI 64, TU 64). The polarization measurements were repeated with thinner targets so that the average proton beam energy (GR 70) compares more closely with that for the cross-section data. These data were again retaken (KA 71) at RHEL in an experiment which included cross-section and asymmetry measurements on the strong inelastic states of some of the same nuclei.

Optical model searches were done by the RHEL group (BA 64) and later by G. R. Satchler (SA 67) and G. W. Greenlees (GR 66, GR 70) in separate attempts to extract optical model parameters from the data in a consistent manner.

None of the studies reported at 30 MeV proton energy include the ^{124}Sn nucleus. Elastic cross section and polarization data have been collected and searches have been done over the tin isotopic sequence, including ^{120}Sn and ^{124}Sn at 39.6 MeV (BO 68). The 39.6 MeV data, the RHEL data and data from other sources at these, and at other energies were combined. A search was conducted on all the collected data testing various analytic expressions for the optical model parameters by E. D. Becchetti and G. W. Greenlees (BGOM) (BE 69). The result of this search was a set of best fit formulas from which optical model parameter values may be calculated for any nucleus in the range A = 40 to 208 and for energies at least up to 40 MeV.

The results of this search are expected to produce the most consistent relationship between the optical model parameters used in the calculations for ^{120}Sn and ^{124}Sn. Other sets of parameters have been tried and calculations with one set (GR 70) are also presented here.

The formulas for the BGOM parameters are

$V_R = 54. - 0.32E + 0.4Z / A^{1/3} + 24.0(N - Z) / A$

$r_R = 1.17$

$a_r = .75$

$W_V = .22E - 2.7 \geq 0$

$W_{SF} = 11.8 - 0.25E + 12.0(N - Z) / A$

$r_I' = r_I = 1.32$

$a_I' = a_I = .51 + .7(N - Z) / A$

$V_{so} = 6.2$

$r_{so} = 1.01$

$a_{so} = .75$

The values obtained from these formulas for ^{120}Sn at 30 MeV are compared with the values obtained from other searches in Table 4.1. In general, the values of a given parameter do not differ greatly from one another. The main deviation between separate parameter sets is seen in

TABLE 4.1 OPTICAL MODEL PARAMETERS

^{120}Sn	V_R(MeV)	r_R(F)	a_R(F)	W_V(MeV)	W_{SF}(MeV)	r_I(F)	a_I(F)	V_{so}(MeV)	r_{so}(F)	a_{so}(F)
BE 69 (BGOM)	52.46	1.17	.75	3.9	6.3	1.32	.627	6.2	1.01	.75
GR 70_1	51.39	1.158	.772	2.62	6.09	1.326	.696	6.25	1.005	.728
GR 70_2	48.18	1.177	.756	.01	7.94	1.217	.956	5.71	1.031	.684
GR 70_3	51.21	1.176	.706	2.34	7.11	1.309	.679	5.71	1.031	.684
SA 67_1	51.4	1.172	.713	2.07	7.47	1.301	.684	6.50	1.067	.828
SA 67_2	51.5	1.168	.720	2.57	7.53	1.314	.650	6.17	1.159	.744
SA 67_3	51.0	1.177	.718	2.21	7.30	1.312	.675	6.35	1.056	.744
KA 71_1	50.4	1.174	.806	0.0	13.78	1.294	.574	5.656	1.083	.652
KA 71_2	49.0	1.184	.80	0.0	13.55	1.304	.567	5.55	1.184	.80
^{124}Sn										
BE 69 (BGOM)	53.05	1.17	.75	3.9	6.62	1.32	.645	6.2	1.01	.75

the various distributions of the absorbtive strength in the surface and volume parts of the absorbtive (imaginary) well.

4.3 Collective Model Calculations

Collective model DWA calculations have been done for the spin flip probability on ^{120}Sn and ^{124}Sn using the best fit optical model parameters of E. D. Becchetti and G. W. Greenlees. Also, cross section and asymmetry calculations done with these parameters are compared to the Karban (KA 71) data on ^{120}Sn.

The effects of using another set of optical model parameters are also presented in this section for all the ^{120}Sn data. The set is GR 70 #3 in Table 4.1.

The results of collective model calculations for spin flip for ^{120}Sn and ^{124}Sn are seen in Figures 4.1 and 4.2. Due to the macroscopic nature of the collective model, significant isotopic differences in the calculations for two such similar nuclei are neither expected nor seen. The collective model correctly predicts the value of the backward angle peak for both ^{120}Sn and ^{124}Sn and is in general agreement with the data at forward angles.

The three curves displayed in Figures 4.1 and 4.2 use the deformed full Thomas spin orbit potential for values of the spin orbit deformation parameter β_{so} of 0, 1β and 2β. The spin flip calculations are not very

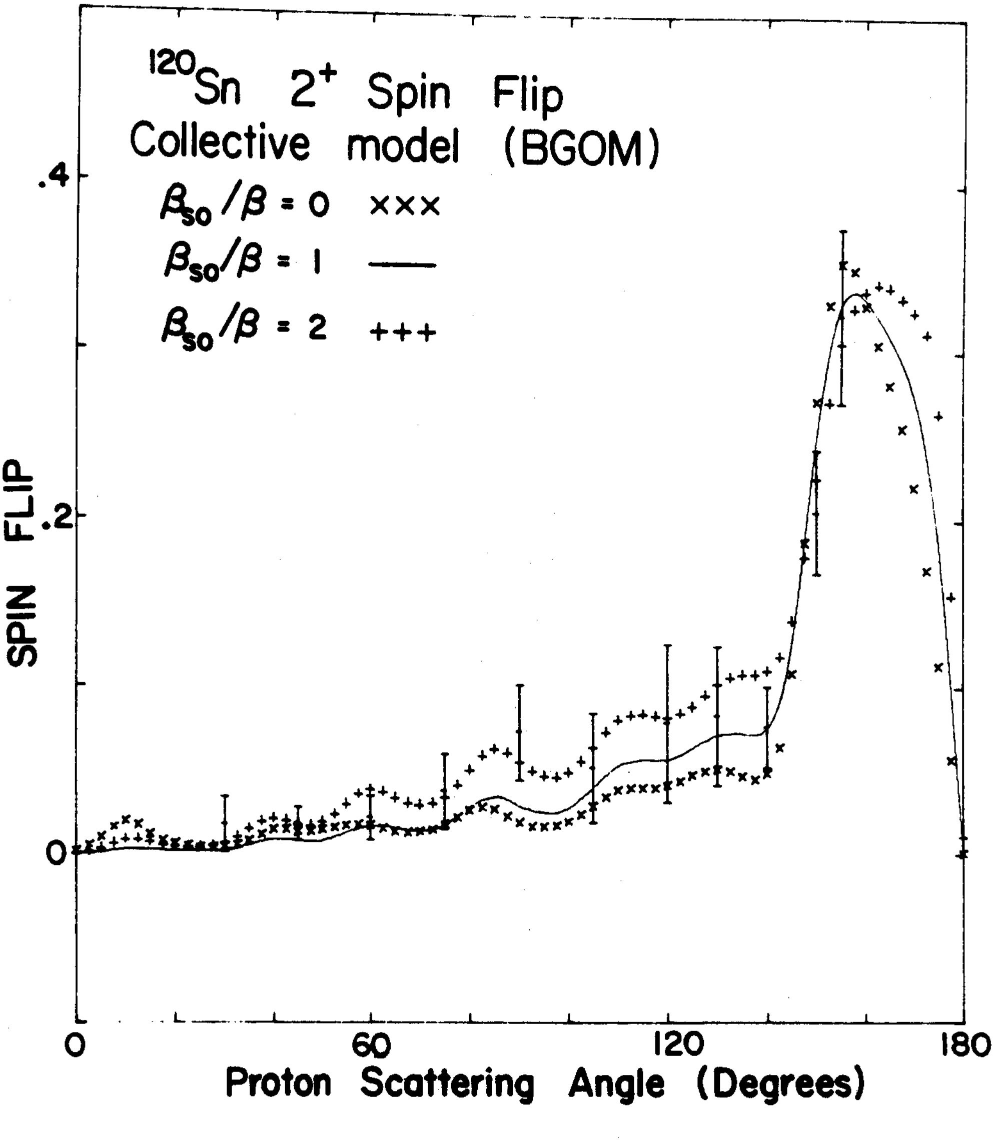

Figure 4.1 Collective model calculations of the ^{120}Sn spin-flip including the deformed spin orbit with the BGOM.

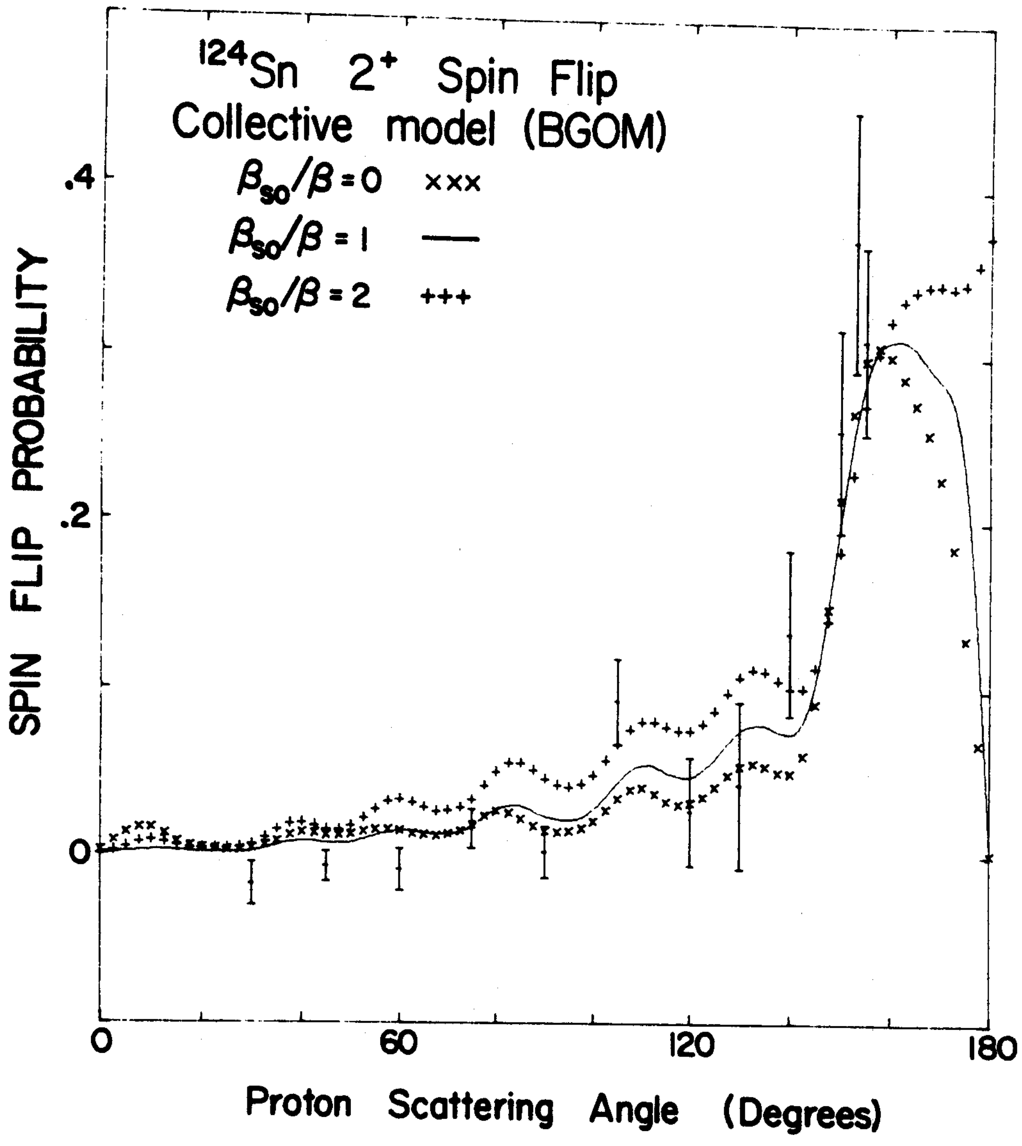

Figure 4.2 Collective model calculations of the ^{124}Sn spin-flip including the deformed spin orbit with the BGOM.

sensitive to the parameter β_{so}. Moreover, the calculations are most sensitive in the angular region when the spin flip values are small. A choice of the value of β_{so} cannot be reliably made from comparison to the spin flip data alone.

Calculations which are more sensitive to the value of β_{so} are those of the asymmetry. Figure 4.3 shows asymmetry calculations for $\beta_{so} = 0$, β and 2β using the BGOM parameters. While varying β_{so} produces some changes in amplitude at the backward angles, a change in the phase of the asymmetry occurs in the forward angles. J. Raynal (RA 71) has suggested that the value of β_{so} is dependent on the detailed structure of the state considered. It will not necessarily be the same as for the central well, however, the best fit to the asymmetry data here clearly is obtained when the value of β_{so} is close to β.

The calculated inelastic cross sections for $\beta_{so} = 0$, β, 2β are seen in Figure 4.4. As in the case of spin flip, the calculated cross sections are not very sensitive to the value of β_{so}. The value of the central well deformation parameter β is 0.133. This is in general agreement with previous results (KA 71, FU 68). This value is about 10% higher than that extracted from experimental BE(2) values (CU 69).

Spin flip calculated with a second optical model parameter set (set GR 70 #3 in Table 4.1) for ^{120}Sn is

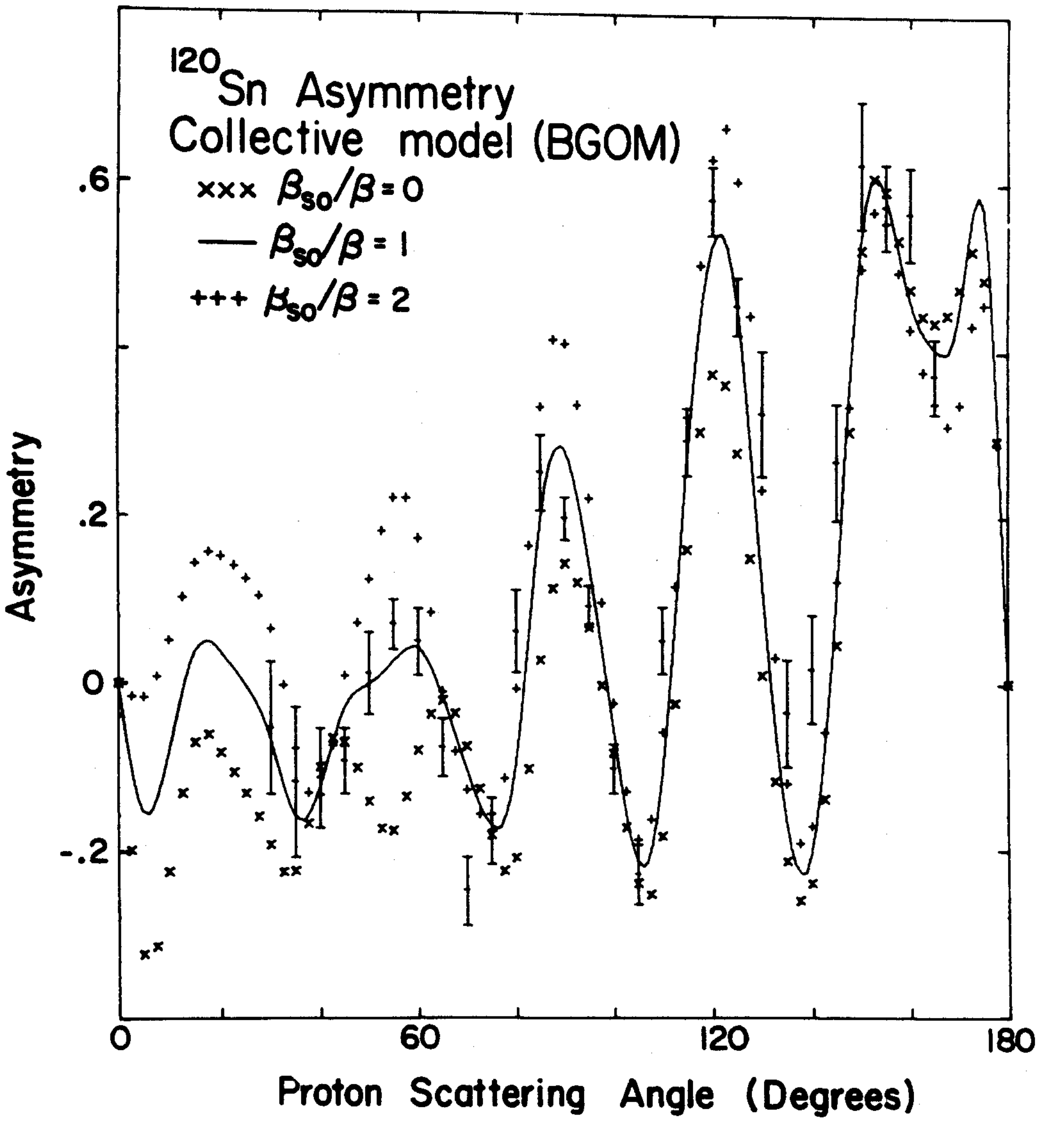

Figure 4.3 Collective model calculations of the ^{120}Sn asymmetry including the deformed spin orbit with the BGOM.

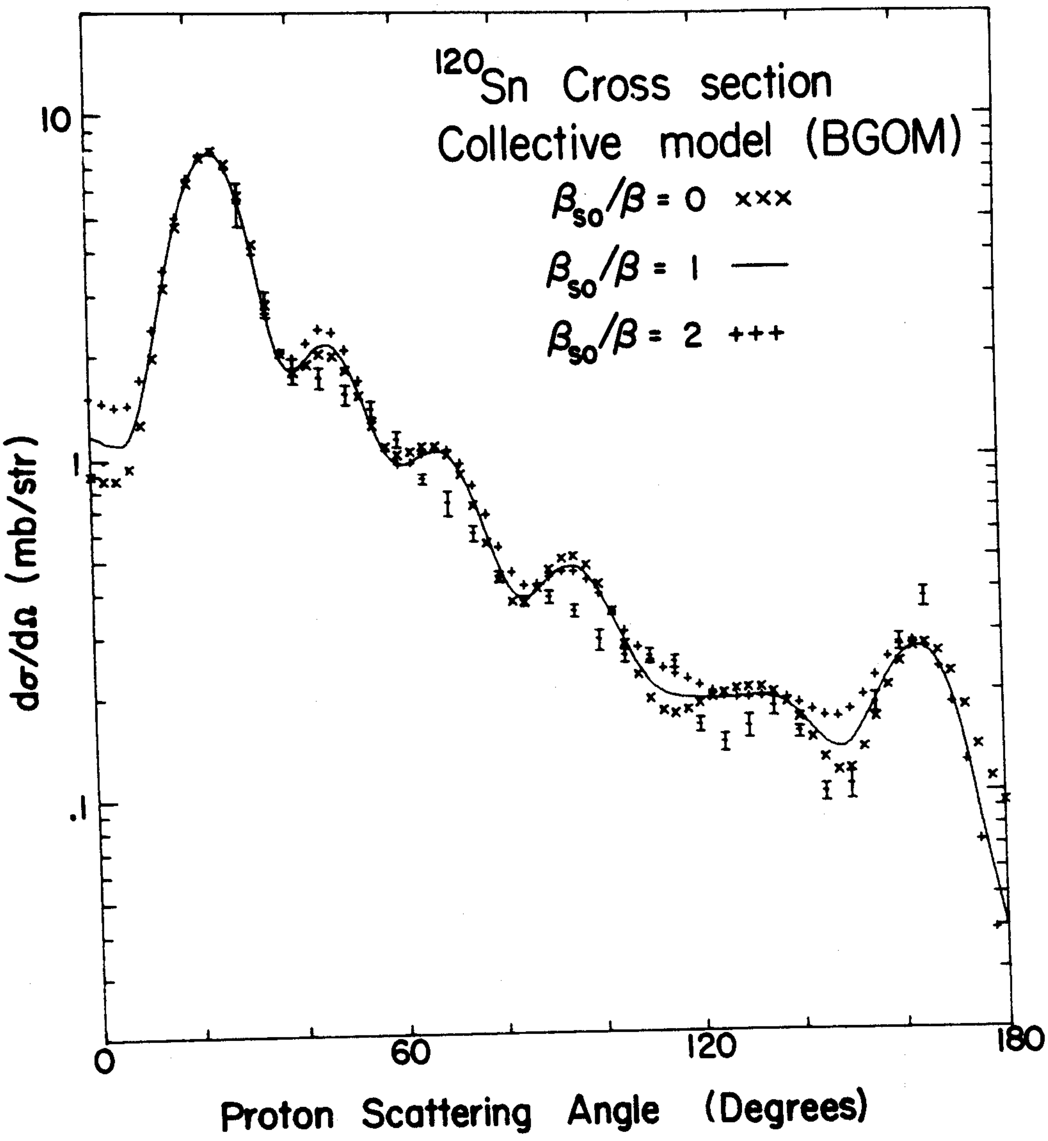

Figure 4.4 Collective model calculations of the ^{120}Sn cross section including the deformed spin orbit with BGOM.

seen in Figure 4.5. The main feature of interest is that while the strength of the spin orbit well of GR 70 #3 is less than that of the BGOM, the value predicted for the backward peak is higher than that predicted by the BGOM. The relationship between the depth of the spin orbit well and the magnitude of the predicted back angle peak is not a straightforward one.

The effects of varying the optical model parameter set on the calculated values of spin flip are interesting. The collective model without a distorted spin orbit term correctly predicts the backward peak. This form of the interaction potential allows no spin flip in the nuclear interaction. Thus, the back angle peak must be the result of spin flip in the elastic channels. It is known that in the absence of spin orbit coupling in the elastic channels that the backward angle peak is not predicted (KO 69). However, the magnitude of the backward angle peak does not depend on the depth of the spin orbit well alone. It also depends on the strength and shape of the other wells and the strength of the full Thomas spin orbit term. Calculations of the asymmetry and cross section with the GR 70 #3 parameters are seen in Figures 4.6 and 4.7, respectively. For either the asymmetry or cross section, agreement with the data is not affected much in using different optical model parameters. The value of $\beta(.127)$ is 5% lower than β from the BGOM calculations.

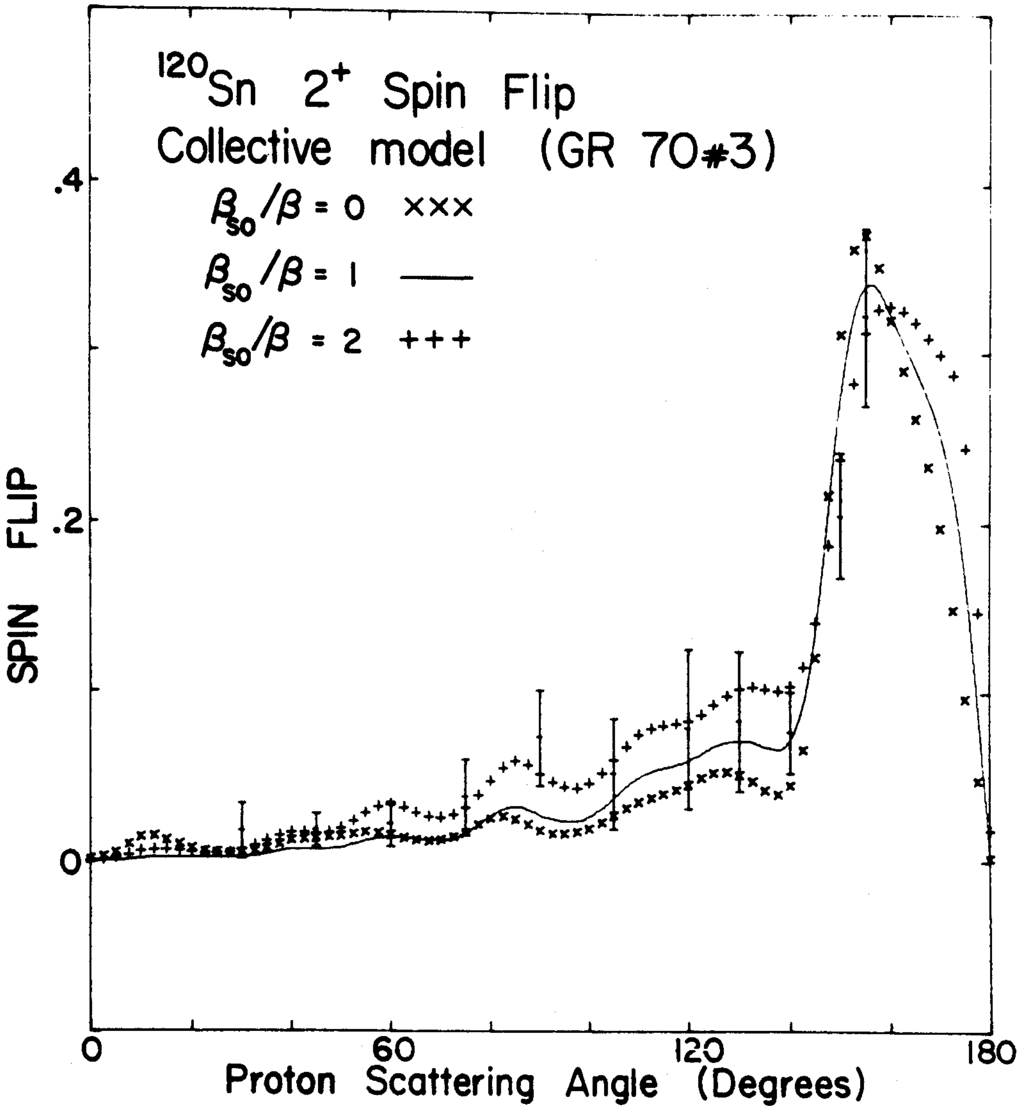

Figure 4.5 Collective model calculations of the ^{120}Sn spin-flip with optical model parameters BG 70 #3.

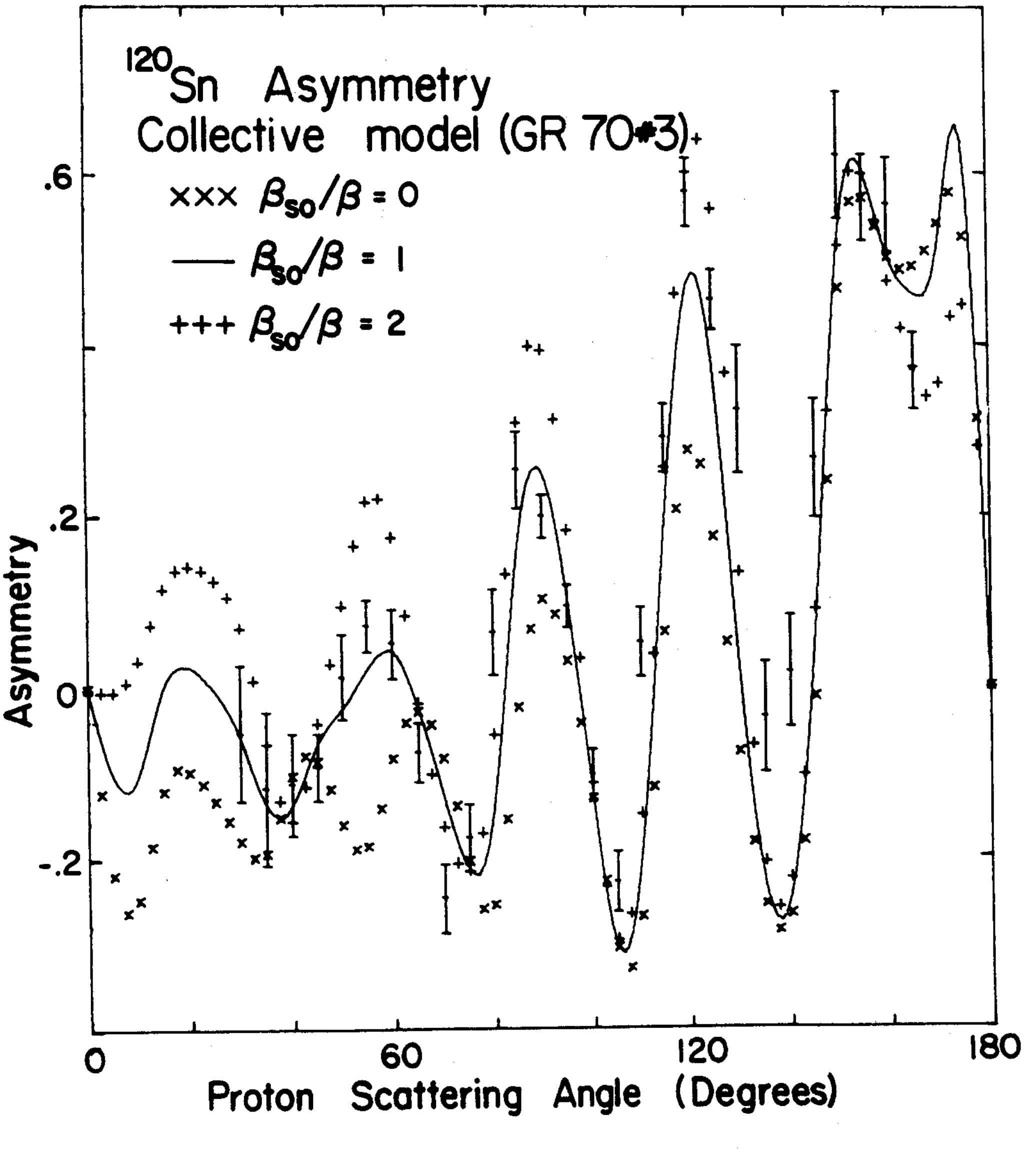

Figure 4.6 Collective model calculations of the ^{120}Sn asymmetry with optical model parameters BG 70 #3.

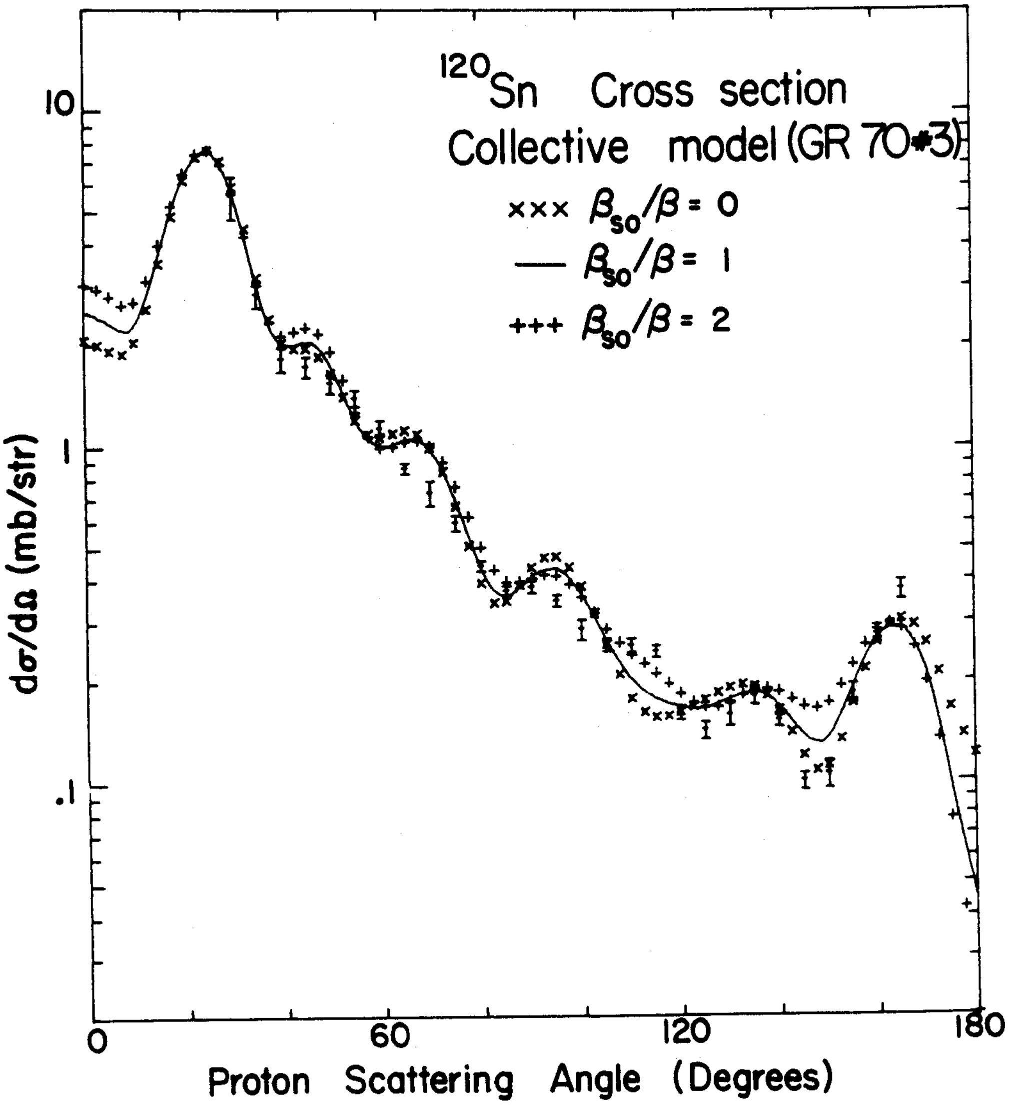

Figure 4.7 Collective model calculations of the ^{120}Sn cross section with optical model parameters BG 70 #3.

4.4 Microscopic Model Calculations

Microscopic model DWA calculations have been done for the spin flip probability on ^{120}Sn and ^{124}Sn using the KK force and the Clement and Baranger wave functions. The optical model parameters used here are the same as in the collective model case, i.e., the BGOM and alternately, GR 70 #3 from Table 4.1. Comparisons are also made to the published cross section and asymmetry data on ^{120}Sn.

The results of the spin flip calculations on ^{120}Sn and ^{124}Sn are presented in Figures 4.8 and 4.9. Exchange is explicitly included in the calculations for both nuclei using the Petrovitch approximation (PE 71). These calculations were repeated for ^{120}Sn including exchange exactly using the code DWBA 70 (SC 69) which is written in the helicity formalism (RA 68). Because of restrictions in the input to DWBA 70, the KK force was not used. Rather, a force of Yukawa form was required. The range used was 1 fermi and the strengths were chosen to produce the same results for the direct calculation as the KK force (PE 71). So, while the comparison is not exact, agreement between the calculations would indicate that the exchange approximation is not in serious error. This is the case for these calculations (Figure 4.8). The difference between the exact and approximate calculations is minor.

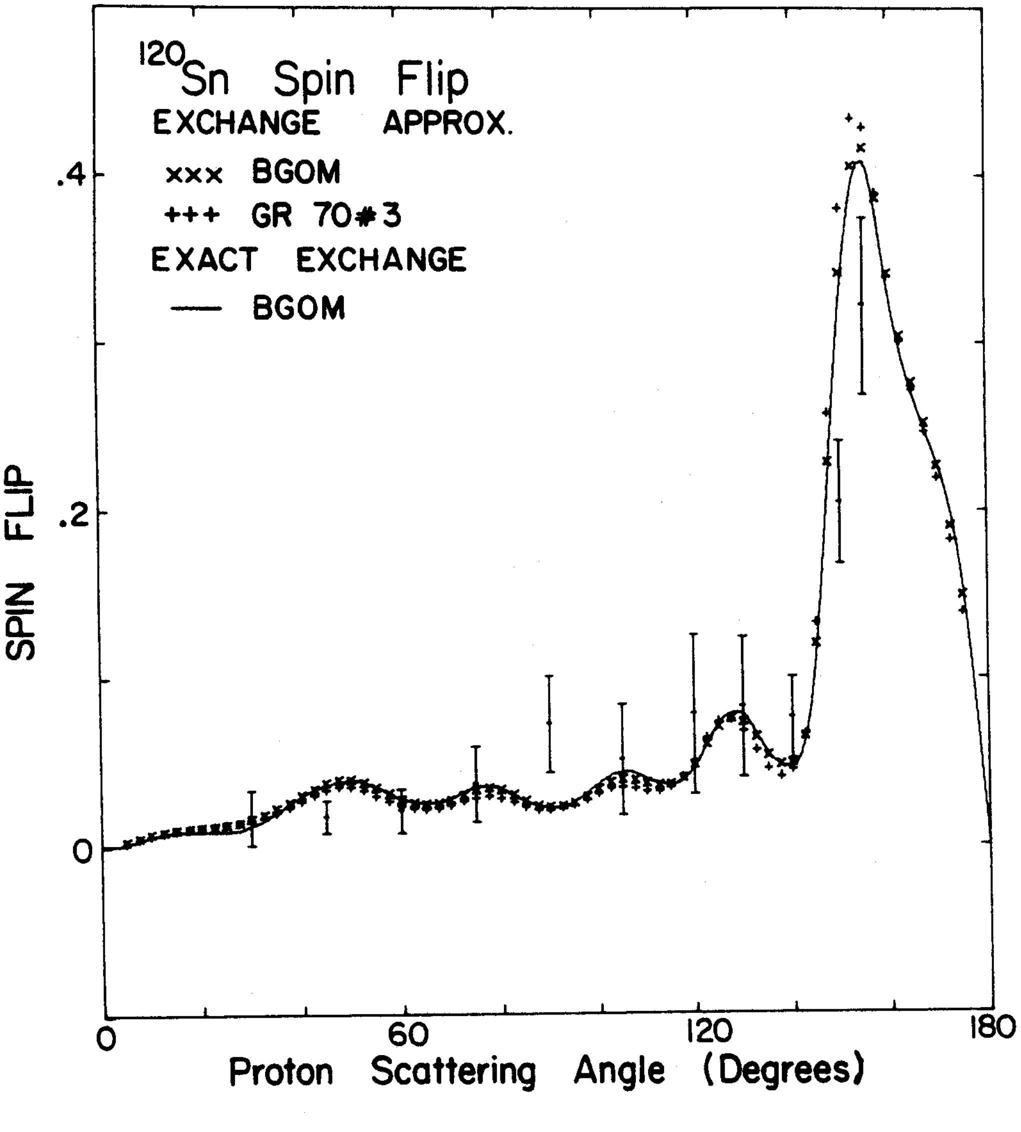

Figure 4.8 Microscopic model ^{120}Sn spin-flip calculations.

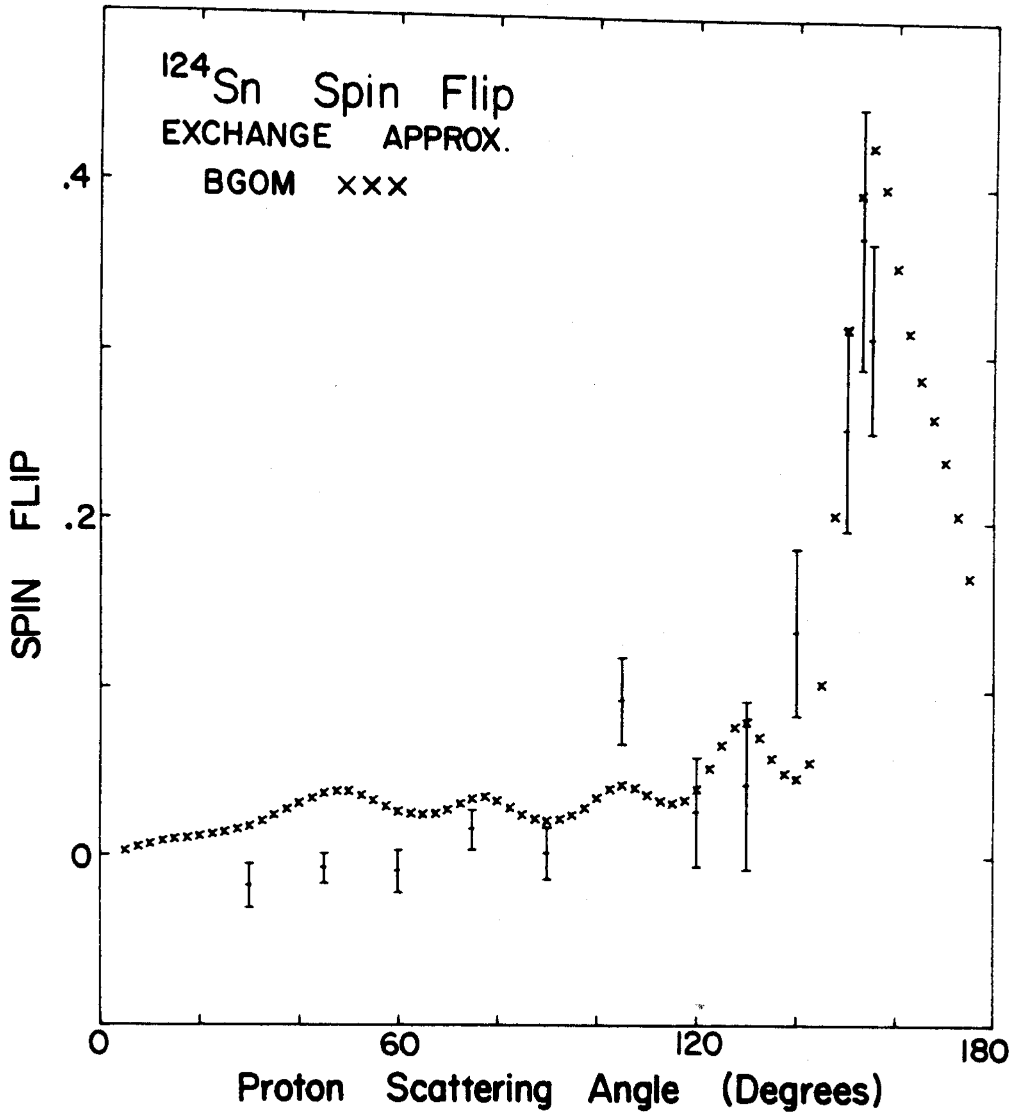

Figure 4.9 Microscopic model ^{124}Sn spin-flip calculations.

The CB wave functions with the KK force predict a spin flip which is in general agreement with the data. The backward peak is somewhat too high for ^{120}Sn, but over all the fits are good.

A microscopic discription of the spin flip interaction might by expected to reproduce the details of isotopic effects in the data. The calculations for ^{124}Sn is not depressed over that for ^{120}Sn at forward angles. An explanation of the lower values of the data for ^{124}Sn does not result from these calculations.

The microscopic prediction of the ^{120}Sn asymmetry is presented in Figure 4.10. The most striking feature of these calculations is how poor the fits are to the data in comparison with the collective model fits. The values are too low throughout the whole angular range of the fit. Only the phase of the oscillations continues to agree with the data. There are two factors included in the collective model case but not in these calculations which might affect this. First, the KK force is central. No spin orbit force is included in the KK force. Second, the KK force is real. The force represented by the collective model is complex and includes a spin orbit term, the strength of which was varied.

The cross section calculation is presented in Figure 4.11. The normalization of the cross section is absolute, containing no effective charge parameterization. With this in mind, the agreement of the cross section calculation

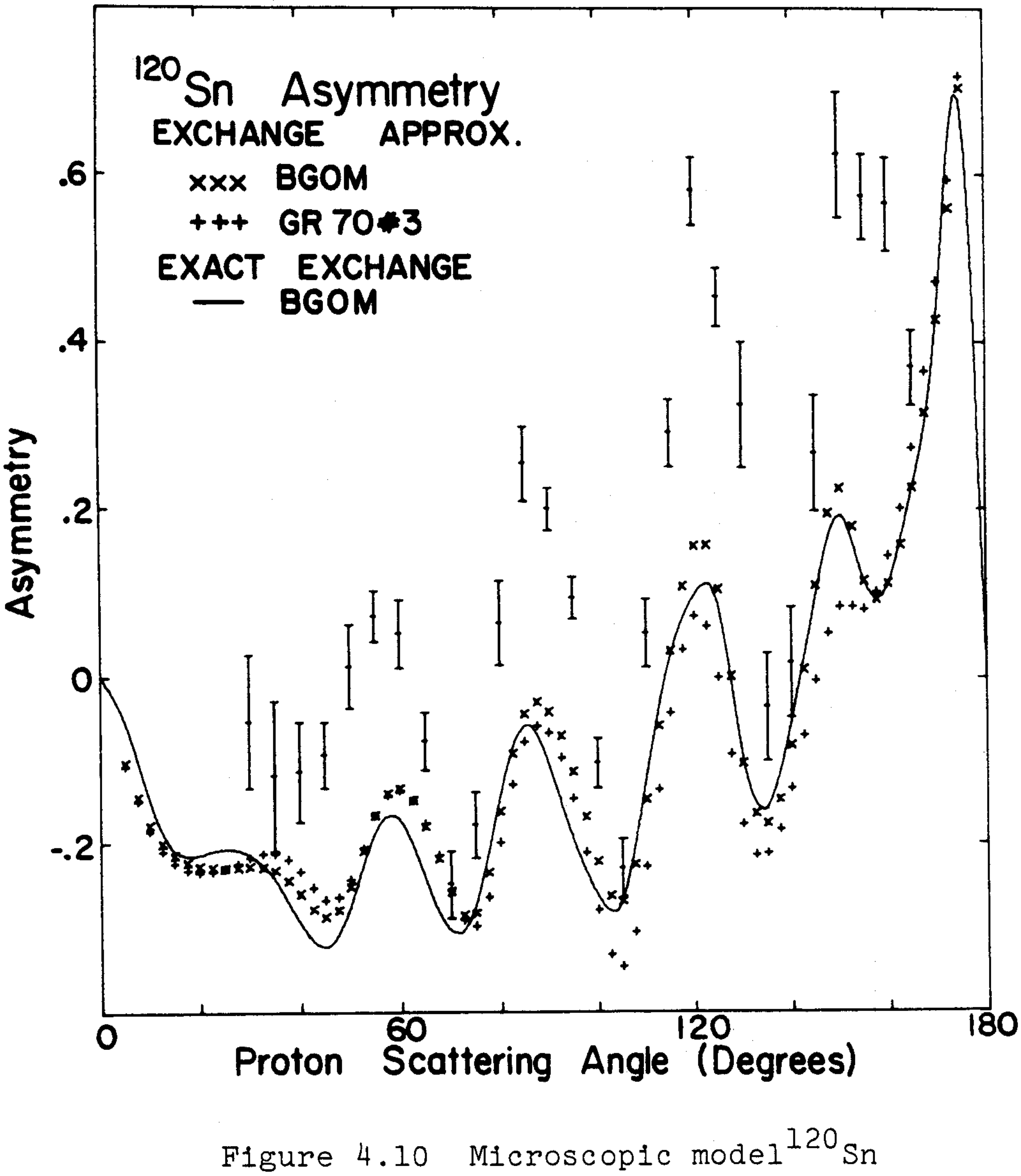

Figure 4.10 Microscopic model ^{120}Sn asymmetry calculations.

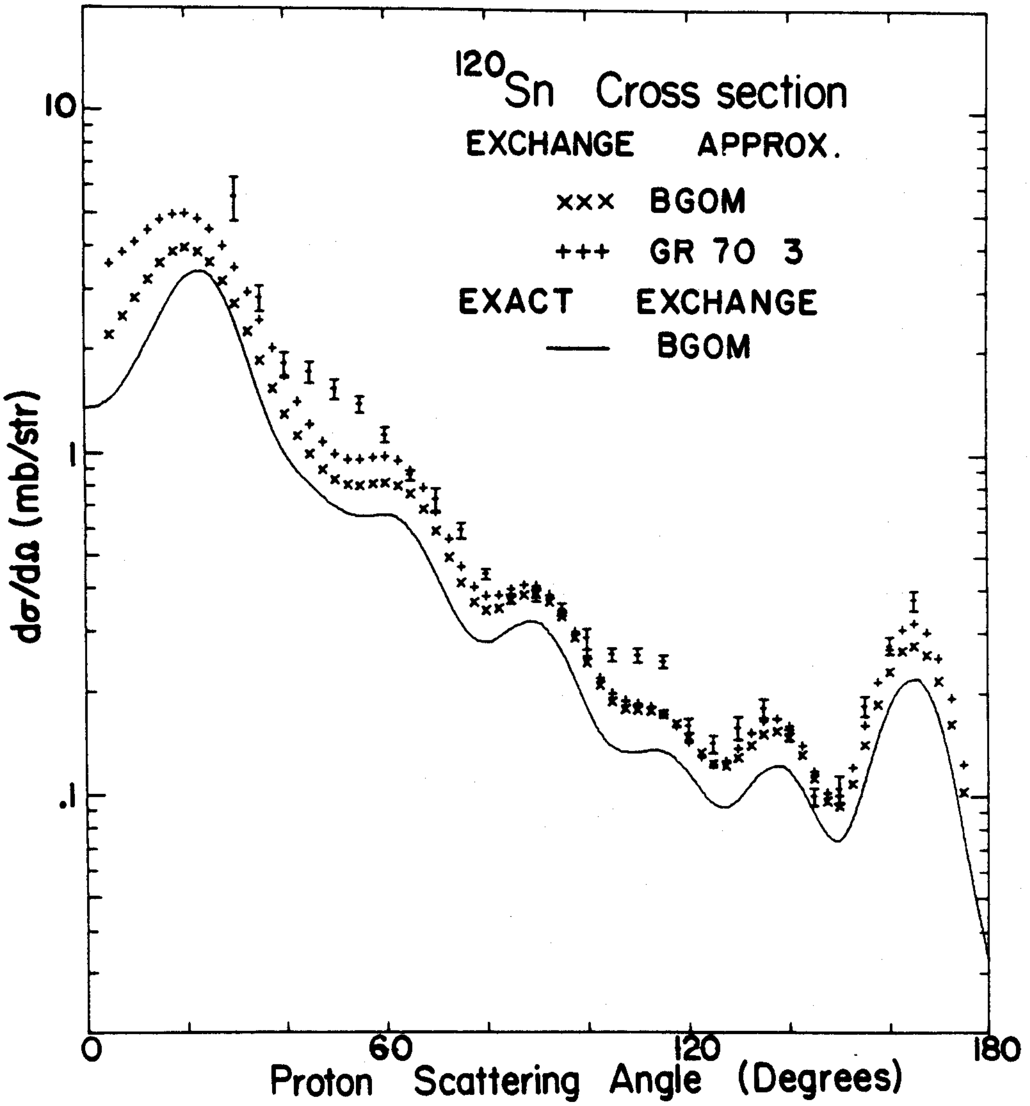

Figure 4.11 Microscopic model ^{120}Sn cross section calculations.

with the data is very good. The cross section is too low at the first maximum, but the shape is in general agreement with the data. The CB wave functions appear to describe the 2^+ state very well. The exchange approximation is also successful here. The approximate and exact calculations are in close agreement.

Included in Figures 4.8, 4.10, and 4.11 are calculations with the CB wave functions and KK force with approximate exchange using the optical model parameter set GR 70 #3. As in the collective model case, varying the optical model parameters does not result in large changes in the calculations. The parameter set with the lower V_{so} strength again predicts a slightly higher value for the backward angle spin flip peak.

To investigate the degraded fit obtained with the microscopic force and wave functions to the asymmetry data, the exact exchange calculation was repeated with a microscopic L·S force included in the interaction. The radial form of the L·S force used is a superposition of two Yukawa forces. The volume integrals of $V(r)\ r^2$ and $V(r)\ r^4$ have been equated to the volume integrals of the Gaussian force of D. Gogny (GO 70) and the strengths and ranges of the Yukawa form determined. The potentials with strengths in MeV and ranges in fermis obtained through this method are (AU 71)

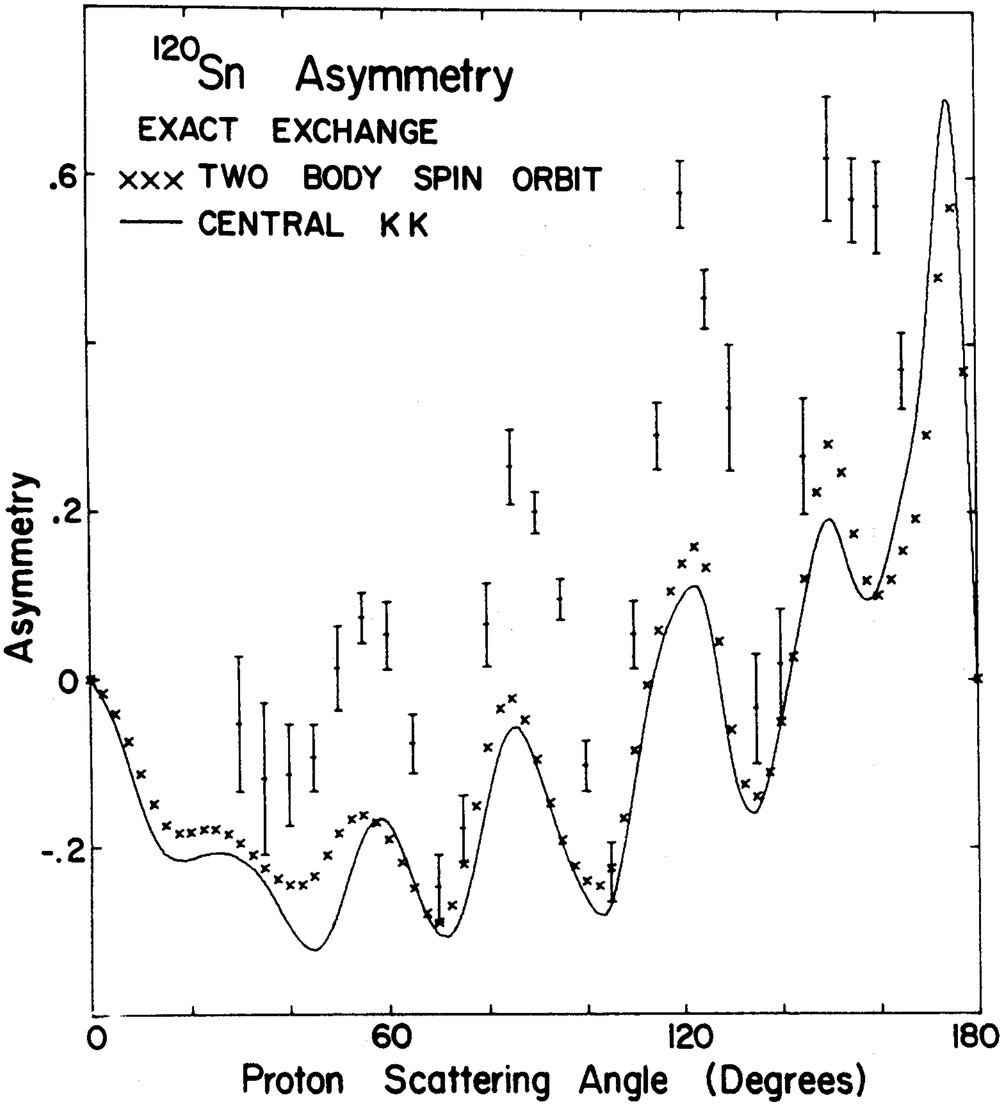

Figure 4.12 Microscopic model ^{120}Sn asymmetry calculations with a two body spin orbit force.

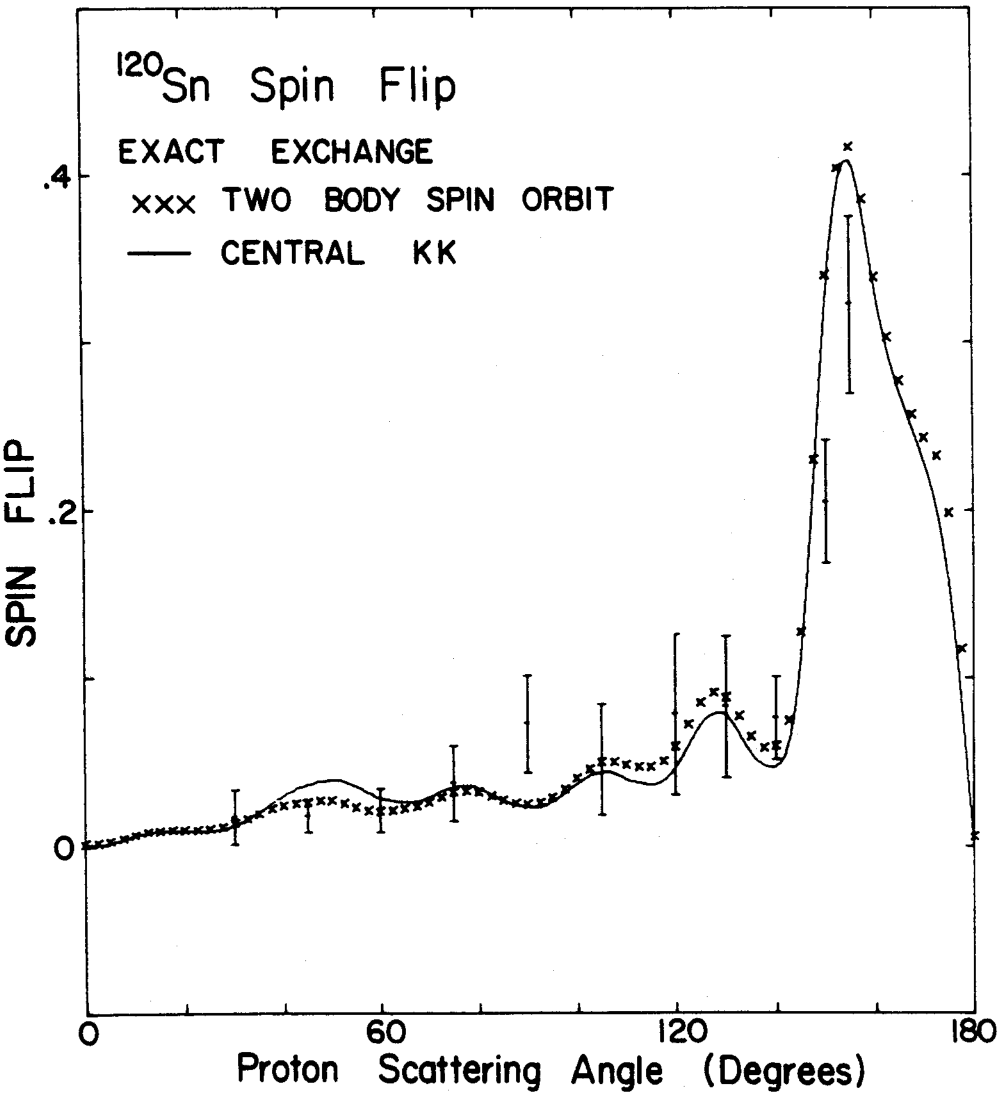

Figure 4.13 Microscopic model ^{120}Sn spin-flip calculations with a two body spin orbit force.

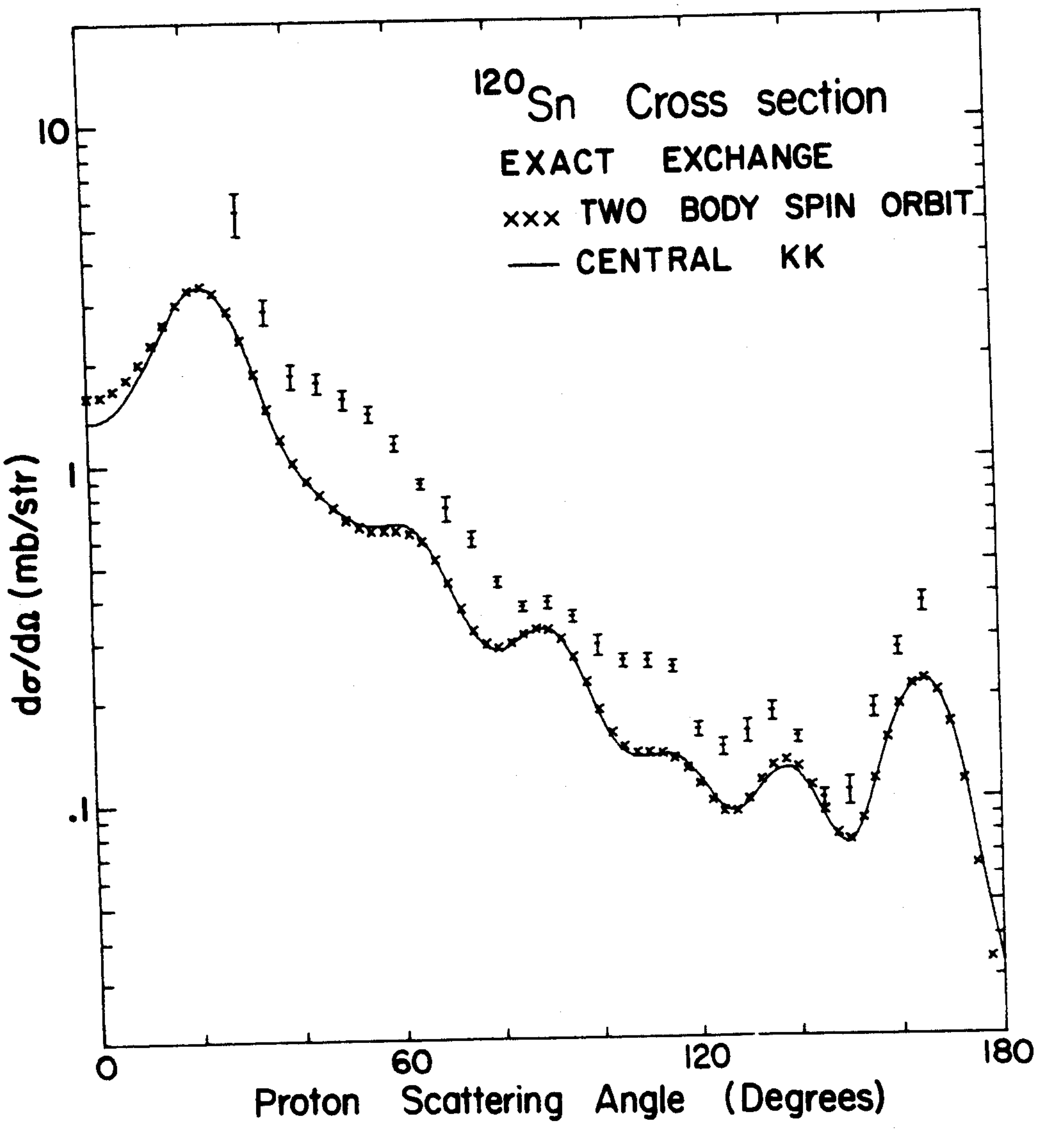

Figure 4.14 Microscopic model ^{120}Sn cross section calculations with a two body spin orbit force.

$$V_{pp} = -574 \exp(.329\ r)\ /\ .329\ r$$

$$V_{pn} = -287 \exp(.329\ r)\ /\ .329\ r + 218 \exp(.238\ r)\ /\ .238\ r \quad .$$

The calculated cross section, asymmetry and spin flip with the KK equivalent central force and spin orbit force are presented in Figures 4.12, 4.13 and 4.14. Including the spin- orbit force does not greatly affect any of the results. W. G. Love has found the L•S force to be important in fitting inelastic scattering to excited states with high spin (6^+, 8^+) in ^{90}Zr at 60 MeV (LO 71). A more complete investigation (LO 71A) showed that for the states of lower spin (2^+, 4^+), the spin orbit contribution to the cross section is not very strong. J. Raynal (RA 68), using a somewhat stronger spin orbit force (J_4 for Raynal is about twice J_4 for Love), found improved agreement in the forward angles of the asymmetry of the lowest 2^+ state in ^{90}Zr at 20.3 MeV. This is not the case for ^{120}Sn when the Gogny L•S force is used.

There are two methods of estimating the imaginary part of the microscopic interaction. A simple-minded approach is to take the collective model imaginary part normalized to the microscopic calculations. A second possible prescription for calculating the microscopic imaginary part is the "frivolous model" suggested by G. R. Satchler (SA 71). The preceding microscopic calculations, including approximate exchange with the CB wave functions and the KK force using the BGOM, have been repeated with each of these imaginary parts. The asymmetry calculations may be seen in Figure 4.15. Also, calculations done with a real collective model form factor including deformed spin orbit are seen.

It is evident that a complex form factor with either imaginary part gives substantial improvement to the asymmetry over the real form factor calculation alone. Also, one sees from the real collective form factor with deformed spin orbit calculation, that the imaginary term complements the effects of the deformed spin orbit. The deformed spin orbit improves the agreement with the data at forward angles without a corresponding effect over the rest of the angular range. The imaginary part has least effect at forward angles, producing better agreement over the range of middle and backward angles.

The fits to the cross section are presented in Figure 4.16. Addition of an imaginary part produces a general improvement to the fit. The first maximum is in better agreement, while the rest of the angular range is not changed much. The spin flip calculations are seen in Figure 4.17. While addition of the collective imaginary part did not affect the values of the calculations, the Satchler imaginary part grossly over predicts the value of the backward angle peak. The "frivolous model" clearly produces much worse agreement in this case. It is noteworthy that while the calculations for spin flip seemed

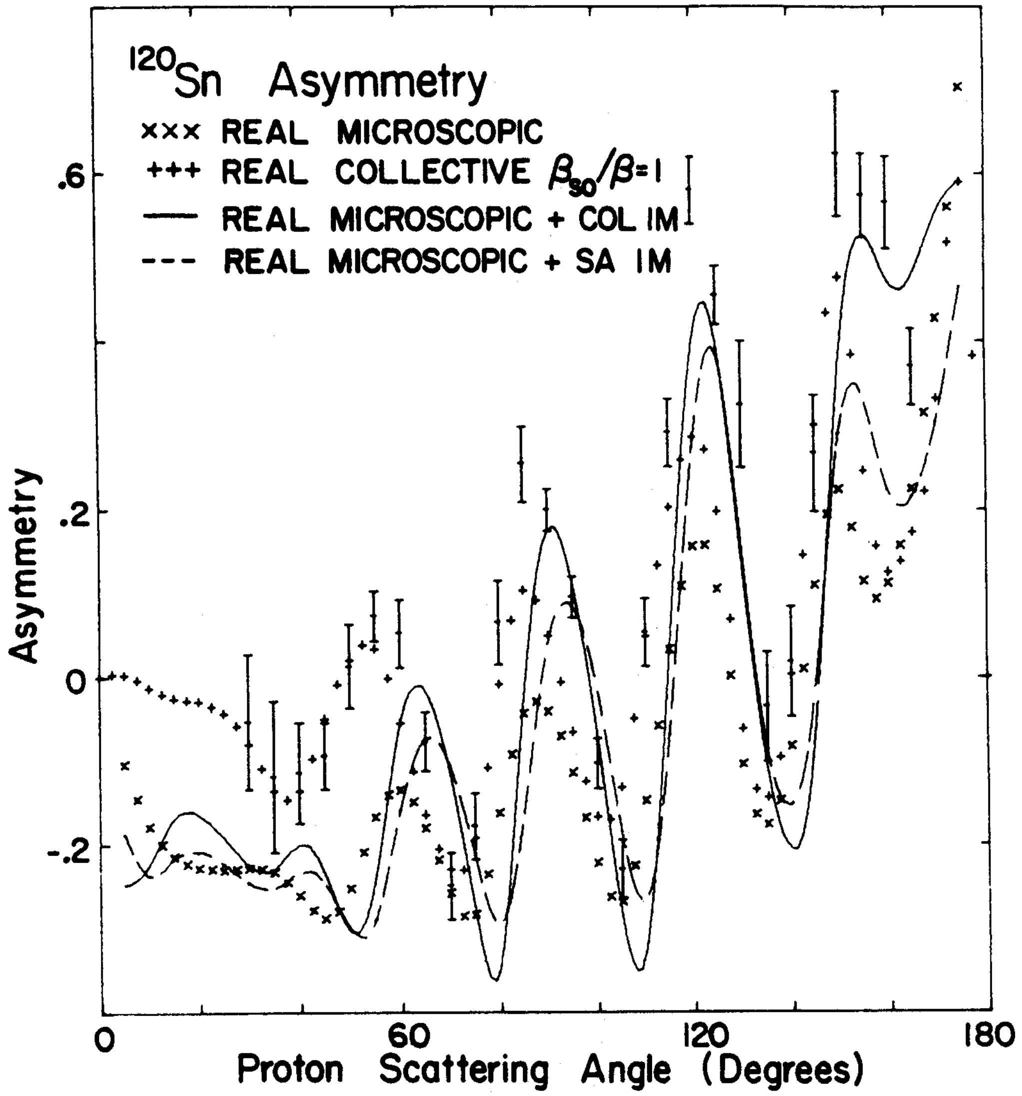

Figure 4.15 ^{120}Sn asymmetry microscopic model calculations including complex coupling.

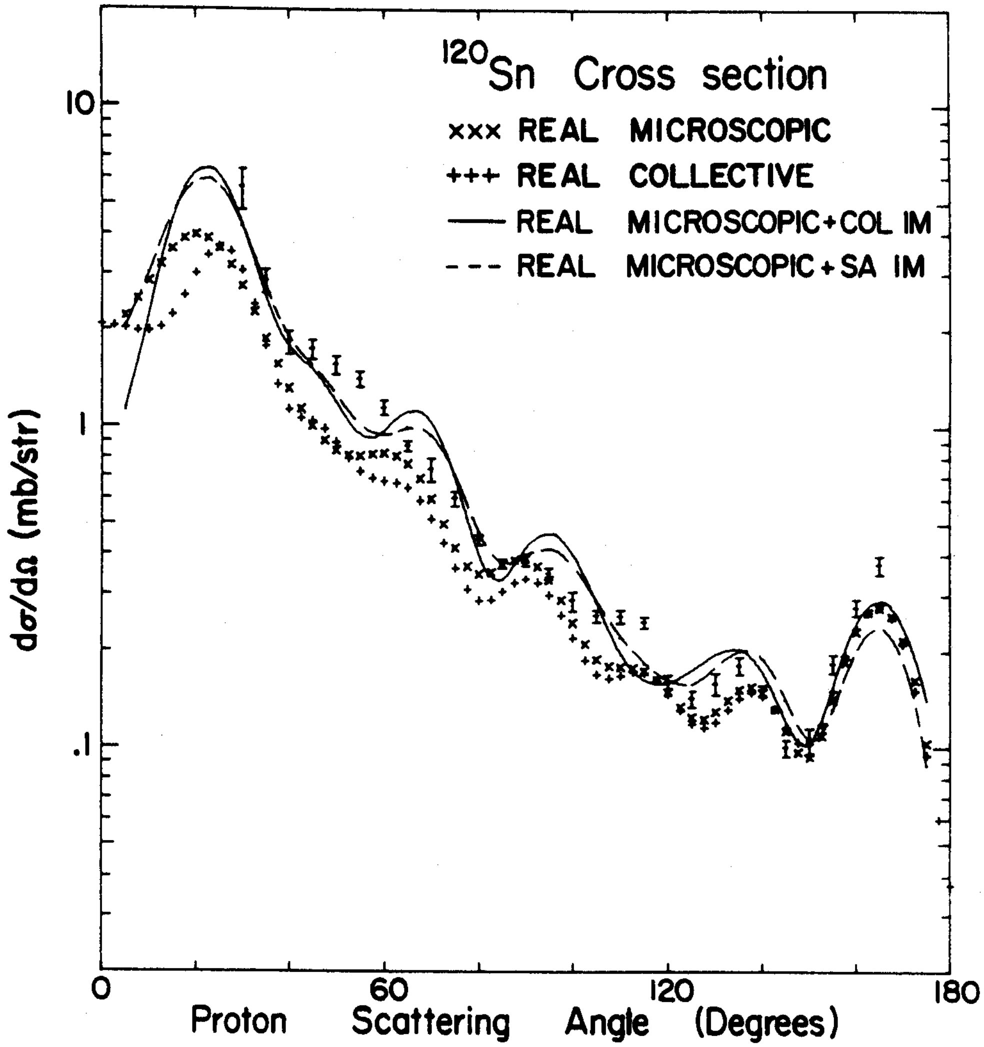

Figure 4.16 ^{120}Sn cross section microscopic model calculations including complex coupling.

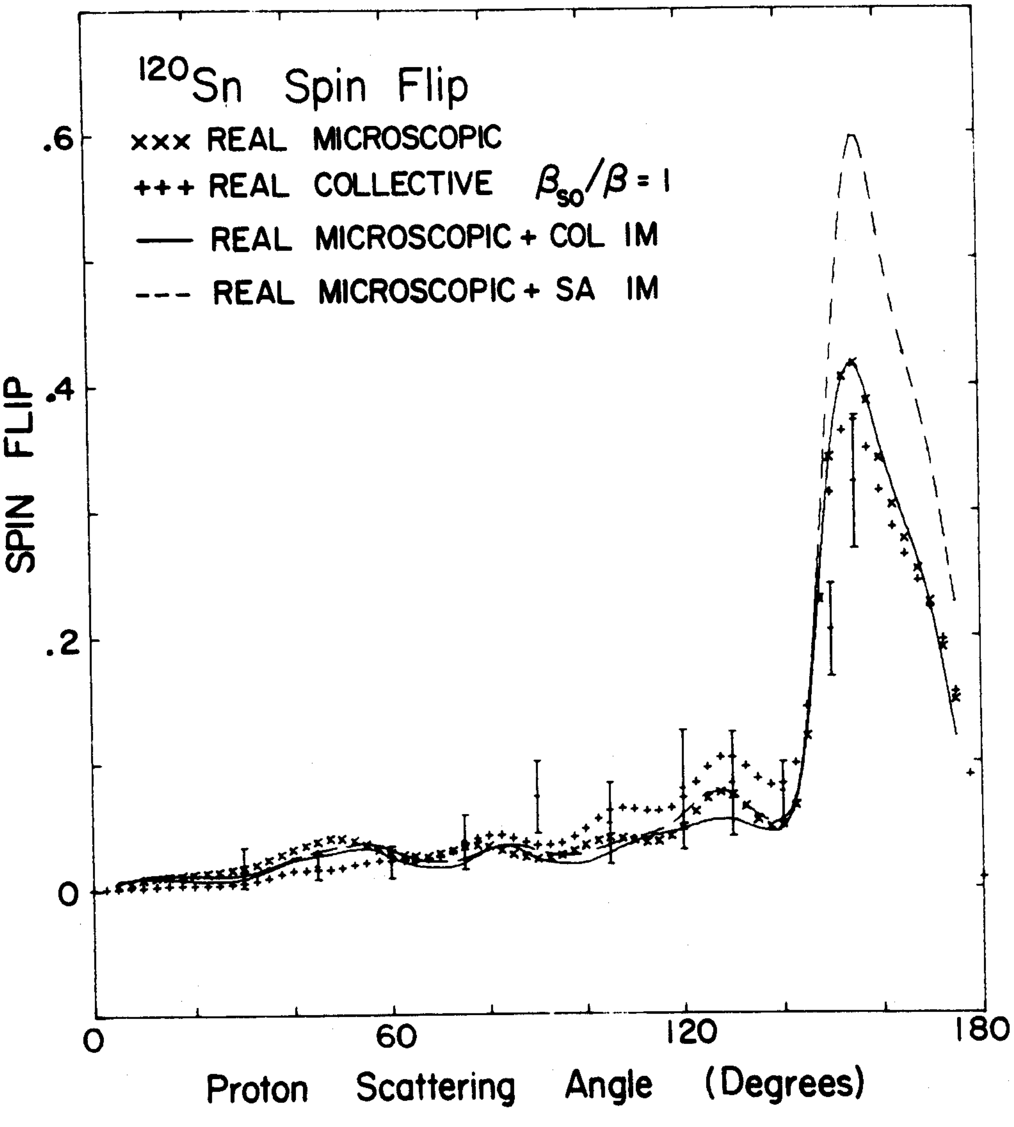

Figure 4.17 ^{120}Sn spin-flip microscopic model calculations including complex coupling.

fairly insensitive to other changes, the Satchler imaginary part produced a pronounced effect.

Calculations studying these complex form factors on other states and a description of the Satchler formulas are found in the Appendix.

5. SUMMARY

Spin-flip probabilities for the excitation of the first 2^+ states in ^{120}Sn and ^{124}Sn have been measured for inelastic proton scattering at 30 MeV. The spin-flip data for both isotopes are quite similar. Both show the peak at back angles which is characteristic in medium energy spin-flip data taken on lighter nuclei. The tin cross section, asymmetry (KA 70) and spin-flip data have been analyzed with both macroscopic and microscopic DWA models.

For the collective model, fits to the cross section are reasonably good. Use of a deformed spin orbit term is important, but no more so than the imaginary part of the collective form factor, for the asymmetry data. Deforming the spin orbit well has little effect on either the spin-flip or cross section calculations. The fit to the ^{120}Sn spin-flip data is quite good over the whole angular range. The fit to ^{124}Sn spin-flip is good for the backward angle peak but the low forward angle values are not predicted. Little structure is predicted or seen in the forward angle spin-flip data for either nucleus.

For the microscopic model, the shape and magnitude of the cross section and spin-flip predictions are quite reasonable. The predicted spin-flip has a higher value at the backward angle peak than for the collective case. However, it still shows agreement with the data.

Isotopic differences were not evident in comparing spin-flip predictions for ^{120}Sn and ^{124}Sn. Use of an approximate exchange term did not result in serious error for either cross section, spin-flip or asymmetry calculations. Including a realistic two body spin orbit interaction potential did not significantly affect the calculations for cross section, spin-flip or asymmetry.

The asymmetry was poorly fit with a real KK interaction. The addition of an imaginary term to the form factor greatly improves the asymmetry prediction and shows some improvement in the fit to the cross section. Of the two imaginary terms used, calculations with the collective imaginary term fit the spin-flip data much better than calculations with the microscopic term. Calculations of the cross section and asymmetry for the lowest lying states of ^{58}Ni and ^{208}Pb were compared to data at 30 MeV proton energy. Addition of an imaginary term always improved the fit to the asymmetry. Both cross section fits were improved by the addition of the collective imaginary term. Only the ^{58}Ni cross section fit was improved by using the microscopic imaginary term.

6. APPENDIX

A number of authors have pointed out that when the collective model is applied to inelastic proton-nucleus scattering it is important to deform the imaginary and spin-orbit wells in addition to deforming the real well (SA 70). G. R. Satchler recently proposed a semi-phenomenological model for the imaginary form factor in microscopic (p,p') calculations (SA 71). Also, it is now possible to include a two body spin orbit term in microscopic calculations (SC 69, LO 71A). One such calculation for ^{120}Sn is described in Chapter 4.

In view of this it is useful to study the effects of complex coupling on cross sections and asymmetries and to compare the results with those of similar calculations which include a spin orbit term.

Calculations were performed for the lowest lying excited states in ^{58}Ni, ^{120}Sn, and ^{208}Pb using in each case a microscopic real form factor and each of two models for the imaginary form factor. Spin orbit contributions were calculated with the collective model.

The calculations were done in DWA for 30 MeV incident protons using the BGOM parameters. Exchange effects were included explicitly (PE 69). Angular distribution and asymmetry data are from (KA 70), the spin-flip data from this work.

The real part of the microscopic form factor (RFF) in DWA for a normal parity transition is

$$\mathrm{Re}\ F^{JOJ}(r) = \int V^{JO}(r,r_o)g_J(r_o)r_o^2dr_o \tag{6.1}$$

where V^{JO} is the Jth multipole of the projectile-target interaction, which in these calculations was chosen to be the long range part of the Kallio-Kolltveit potential.

The function g_J is the transition density. It was assumed that the g_J's had the same form as charge transition densities used to calculate inelastic electron scattering form factors. These may be inferred from experimental data (CU 69), BA 67, HI 70, DU 67).

$$g_J(r) = (A/Z) \quad \rho_{CHARGE}(r) \tag{6.2}$$

Transition densities also can be obtained from theoretical wave functions. A calculation of this sort was described for the 2^+ state in ^{120}Sn in Chapter 4.

Satchler's microscopic imaginary form factor (IM) is

$$\mathrm{Im}\ F_{SA}^{JOJ}(r) = -\frac{W(r)g_J(r)}{\rho(r)} \tag{6.3}$$

where W(r) is the imaginary part of the optical potential and $\rho(r)$ is the ground state matter density with the forms

$$W(r) = (W_V - 4a_I W_S \frac{d}{dr}) f(r,R_I,a_I)$$

and

$$\rho(r) = (1+w(r/c)^2)f(r,c,z)$$

with

$$f(r,x,y) = [1+\exp((r-x)/y)]^{-1}$$

and $R_I = r_I A^{1/3}$. Values of the parameters for the ground state densities (CU 69, BE 67, HA 57) are shown in Table 6.1. Values of the parameters for the optical potentials were taken from the BGOM.

The collective model IM is

$$\text{Im } F^{JOJ}_{COL}(r) = \frac{\beta_J R_I}{2J+1} \frac{d}{dr} W(r)$$

where the β_J's were obtained by normalizing the collective cross sections to those calculated using g_J's given by (4.2).

The microscopic real and imaginary form factors and the collective model IM for the lowest 2^+ states in ^{58}Ni and ^{120}Sn are shown in Figure 6.1; those for the 3^- state in ^{208}Pb are similar.

It is instructive to examine first the effects of deformed imaginary and spin orbit wells on the asymmetry in a purely collective calculation. Such a calculation for the first 2^+ state in ^{120}Sn is shown in Figure 6.2. Both complex coupling and a spin orbit term are necessary to produce good agreement with the data. The spin orbit contribution is especially important in the forward direction. Inclusion of the IM produces a much improved fit at intermediate and back angles, an effect which is not accounted for by deformation of the real and spin orbit wells alone, even if the spin orbit strength is increased. These same observations hold for the other states studied.

TABLE 6.1 Ground State Charge Density Parameters

	C	Z	W
^{58}Ni	4.25	.566	0
^{120}Sn	5.32	.575	0
^{208}Pb	6.40	.542	.14

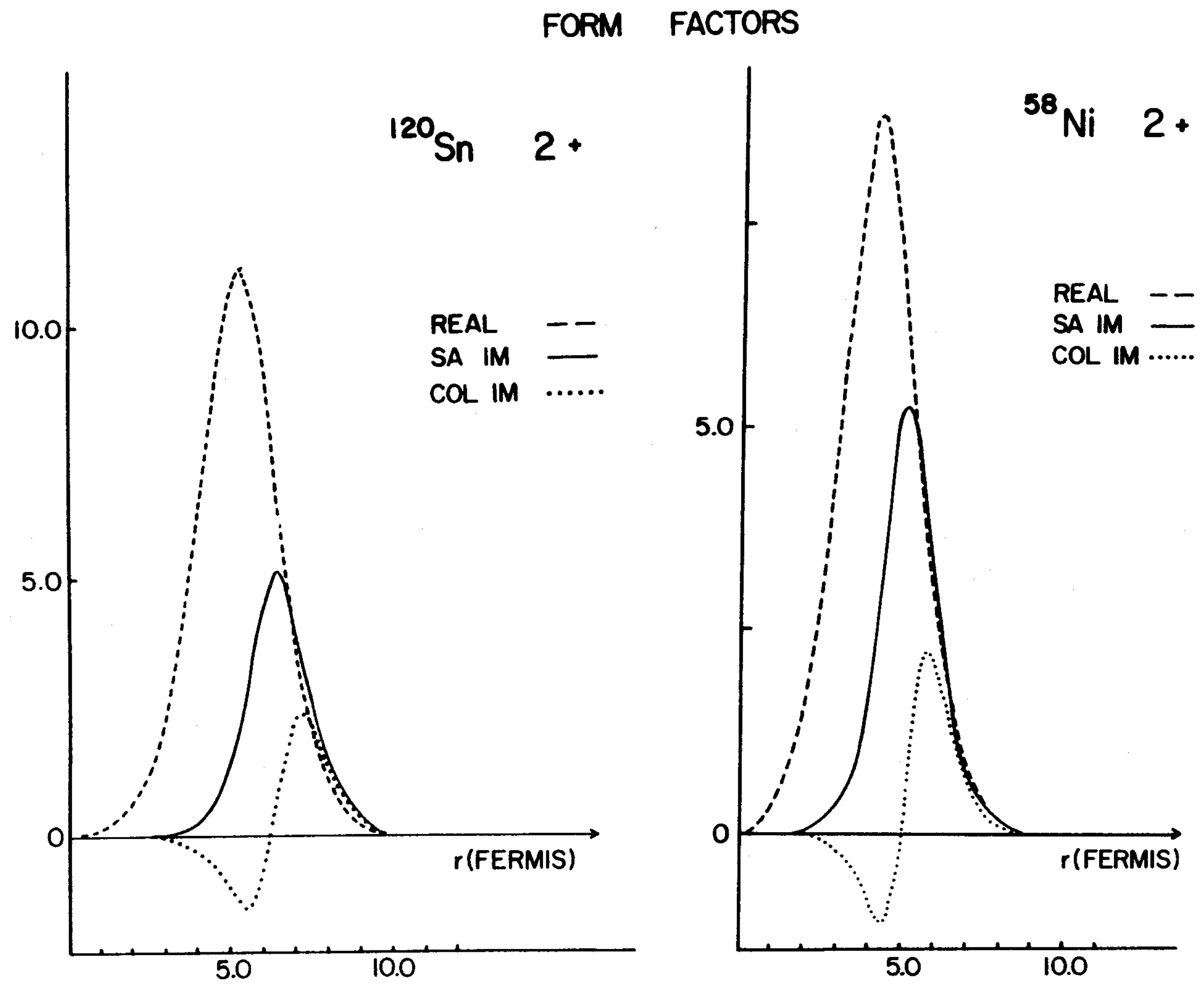

Figure 6.1 Real and imaginary form factors.

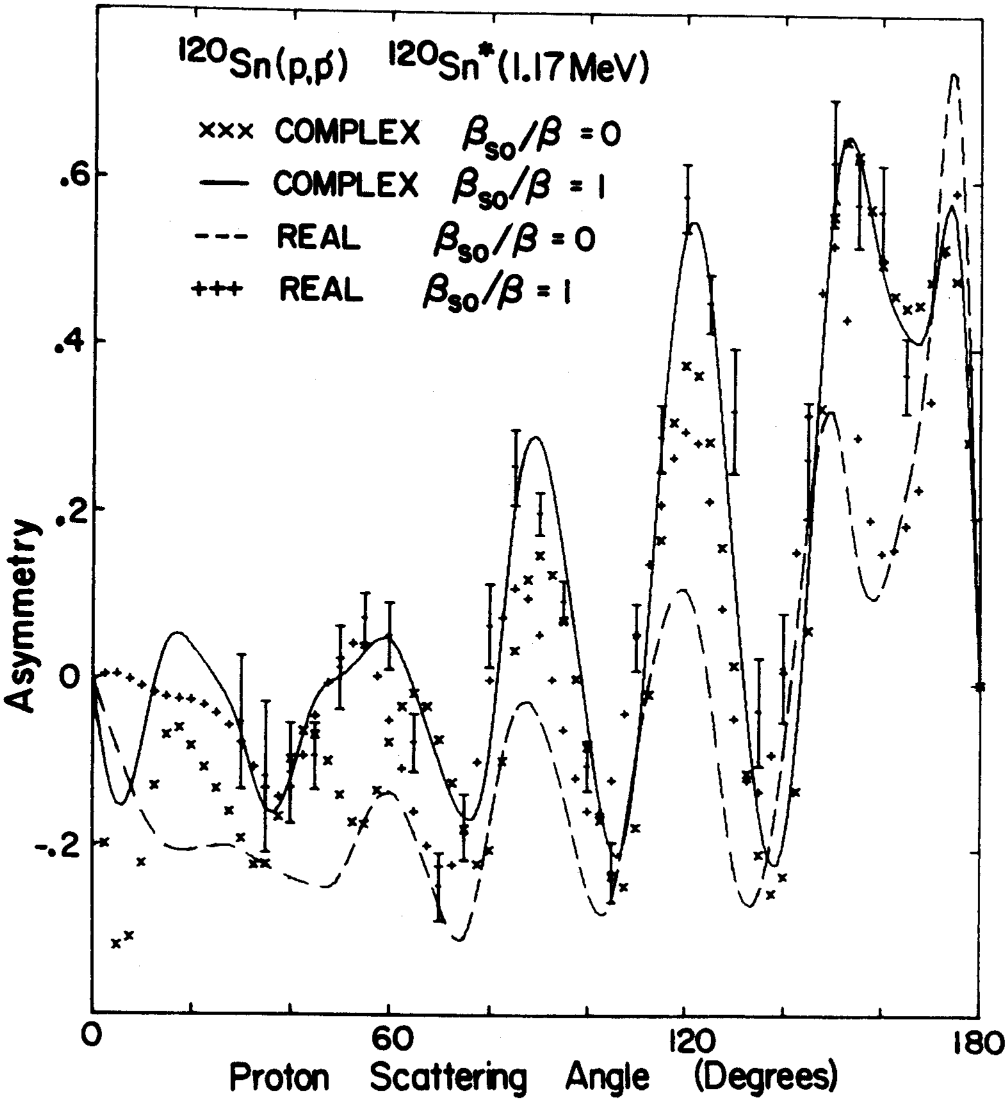

Figure 6.2 ^{120}Sn collective model asymmetry calculations.

Calculations of cross section, asymmetry, and spin-flip for the first 2^+ state in ^{120}Sn are shown in Figure 6.3. The set on the left was done with a transition density extracted from the quasi-particle wave functions of Clement and Baranger. The two real form factors are very similar to each other and to the real collective form factor.

Including either IM improves the fit to the angular distribution in the forward direction and provides a definite improvement in the asymmetry prediction. However, the spin-flip calculations performed with the two IM's differ markedly, the collective IM having little effect, the microscopic IM overestimating the spin-flip at back angles. Since the main features of spin-flip are believed to be determined by the optical potential (SA 70) it appears that in this case the microscopic IM effects undesirable interference among various of the distorted waves.

Calculations for the lowest 2^+ state in ^{58}Ni and 3^- state in ^{208}Pb are shown in Figure 6.4. The effects of complex coupling and the spin orbit term on the ^{58}Ni asymmetry and cross section and the ^{208}Pb asymmetry are similar to those for the 2^+ state in ^{120}Sn. In the ^{58}Ni case including either IM produces little change in the spin-flip prediction. While the collective IM improves the predicted angular distribution for ^{208}Pb, the microscopic IM overestimates the magnitude at all angles. The

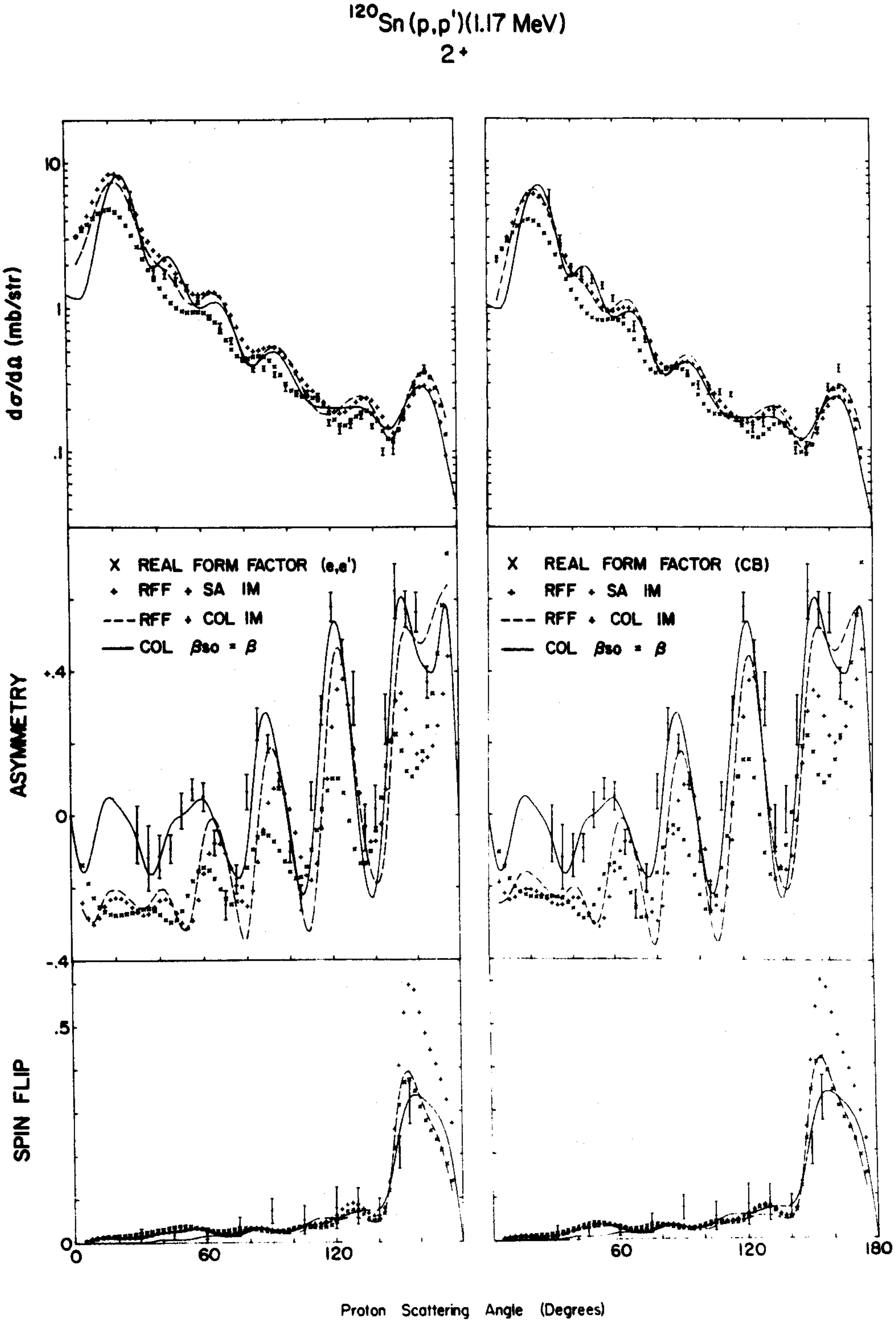

Figure 6.3 ^{120}Sn microscopic calculations including complex coupling.

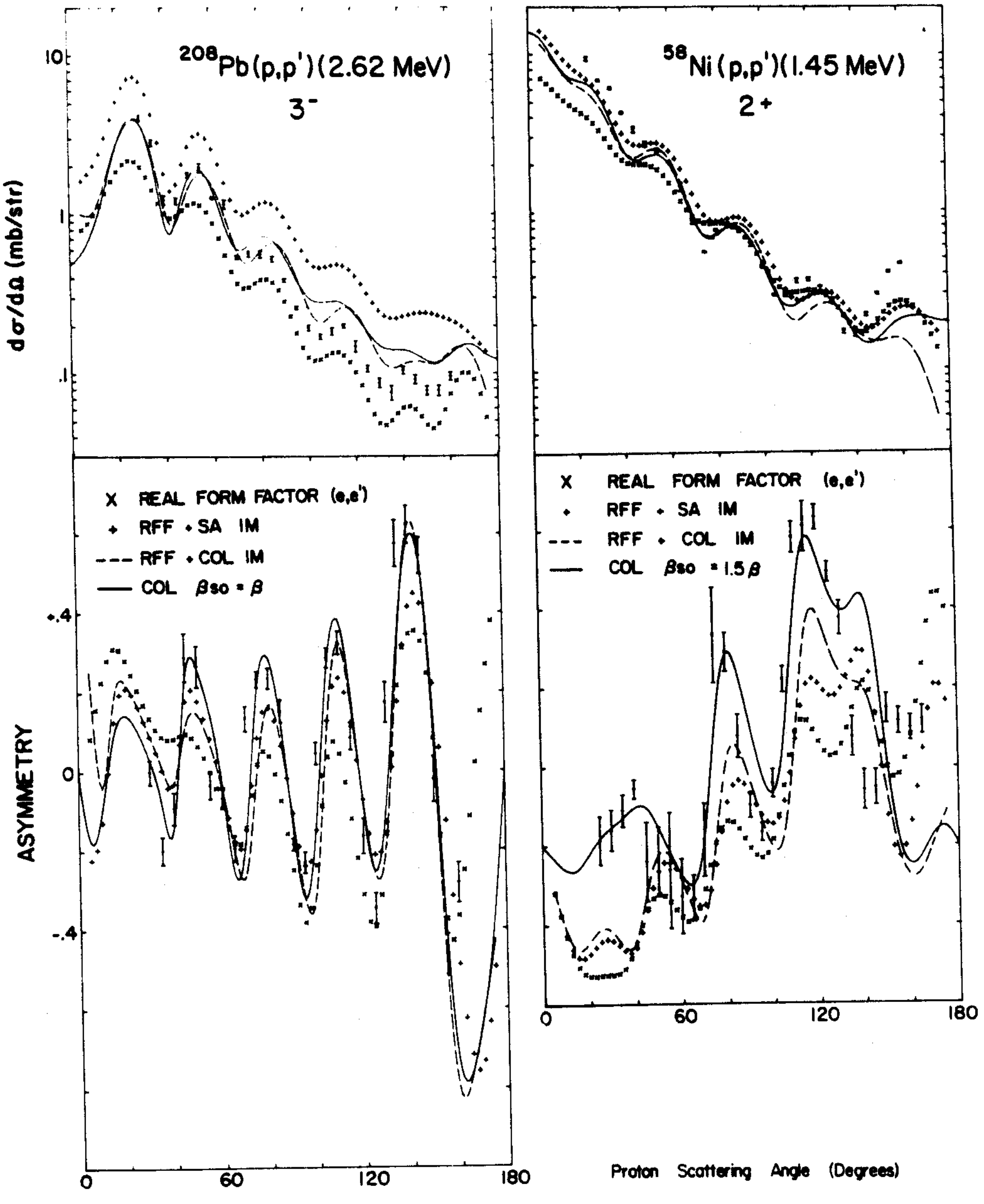

Figure 6.4 ^{208}Pb and ^{58}Ni microscopic calculations including complex coupling.

microscopic IM improves the shape of the fit only at forward angles. The shape at back angles is degraded.

It is evident that complex coupling and a spin orbit term are important for accurate prediction of (p,p') asymmetries. The effects of the two are largely complementary, so that neither alone is sufficient to produce agreement with experimental data.

Complex coupling also has a salutary effect on angular distribution predictions, although, it is not as pronounced as for the asymmetries.

It appears that a collective model spin orbit term has only a slight effect on spin-flip predictions, while the effects of an IM may be pronounced.

The simple collective model IM (6.4) seems to be more reliable than the microscopic prescription (6.3).

LIST OF REFERENCES

AH 70 M. Ahmed, J. Lowe, P.M. Rolph and O. Karban, Nucl. Phys. A147, 273 (1970).

AU 69 R. Au, Michigan State University Cyclotron Laboratory, Sigma 7 Program Description 0012 (unpublished, 1969).

AU 71 S. Austin, private communication.

BA 60 M. Baranger, Phys. Rev. 120, 957 (1960).

BA 64 R.C. Barrett, A.D Hill and P.E. Hodgson, Nucl. Phys. 62, 133 (1964).

BA 67 P. Barreau and J.B. Bellicard, Phys. Rev. Lett. 19, 1444 (1967).

BA 69 D.M. Bayer, Michigan State University Cyclotron Laboratory, Sigma 7 Program Description 0013 (unpublished, 1969).

BE 67 J.B. Bellicard and K.J. van Oostrum, Phys. Rev. Lett. 19, 242 (1967).

BE 69 E.D. Becchetti and G.W. Greenlees, Phys. Rev 182, 1190 (1969).

BL 66 H.G. Blosser and A.I. Galonsky, IEEE Trans. Nucl. Sci., NS-B, No. 4, 466 (1966).

BO 59 A. Bohr, Nucl. Phys. 10, 486 (1959).

BO 68 R.N. Boyd and G.W. Greenlees, Phys. Rev. 176, 1394 (1968).

BR 68 D.M. Brink and G.R. Satchler, Angular Momentum (Clarendon Press, Oxford, 1968).

CL 68 D.M. Clement and E.U. Baranger, Nucl. Phys. A120, 25 (1968) and private communication.

CO 70 V. Comparat, Thesis (University of Paris, France, 1970) unpublished.

CR 64 R.M. Craig, J.C. Dore, G.W. Greenlees, J.S. Lilley and J. Lowe, Nucl. Phys. 58, 515 (1964).

CU 69 T.H. Curtis, R.A. Eisenstein, D.W. Madsen and C.K. Bockelman, Phys. Rev. 184, 1162 (1969).

Du 67 M.A. Duguay, C.K. Bockelman, T.H. Curtis and R. A. Eisenstein, Phys. Rev. 163, 1259 (1967).

EE 71 J. Eenmaa, F.H. Schmidt and J.R. Tesmer, (to be published).

FU 68 S.A. Fulling and G.R. Satchler, Nucl. Phys., A111, 81 (1968).

GI 68 R.O. Ginaven, E.E. Gross, J.J. Malanify and A. Zucker, Phys. Rev. Lett. 21 552, (1968).

GO 70 D. Gogny, P. Pires and R. DeTourreil, Phys. Lett. 32B, 591 (1970).

GR 66 G.W. Greenlees and G.J. Pyle, Phys. Rev. 149, 836 (1966).

GR 70 G.W. Greenlees, V. Hnizdo, O. Karban, J. Lowe and W. Makofske, Phys. Rev. C2, 1063 (1970).

HA 57 B. Hahn, R. Hofstadter and D.G. Ravenhall, Phys. Rev. 105, 1353 (1957).

HE 64 R.L. Heath, Scintillation Spectrometry, Phillips Petroleum Co. IDO 16880 (1964).

HE 69 D.L. Hendrie, C. Glashausser, J.J. Moss and J. Thirion, Phys. Rev. 186, 1188 (1969).

HE 70 J.H. Heisenberg and I. Sick, Phys. Lett. 32B, 249 (1970).

HI 70 H.H. Hippelein, R. Jahr, J.A.H. Pfleger, F. Rott and H.M. Vieth, Nucl. Phys. A142, 369 (1970).

KA 64 A. Kallio and K. Kolltveit, Nucl. Phys. 53, 87 (1964).

KA 70 O. Karban, P.D. Greaves, H. Hnizdo, J. Lowe and G.W. Greenlees, Nucl. Phys. A142, 461 (1970).

KO 69 J.J. Kolata, Thesis (Michigan State University, 1969) unpublished.

KO 69A J.J. Kolata and A. Galonsky, Phys. Rev. 182, 1073 (1969).

KO 69B W.A. Kolasinski, J. Eenmaa, F. H. Schmidt, H. Sherif and J.R. Tesmer, Phys. Rev. 180, 1006 (1969).

LO 71 W.G. Love, Phys. Lett. 35B, 371 (1971).

LO 71A W.G. Love, to be published.

MA 67 G.H. Mackenzie, E. Kashy, M.M. Gordon and H.G. Blosser, IEEE Trans. Nucl. Sci., NS-14 No.3, 450 (1967).

OR 69 Ortec Inc. Instruction Manuel for the 442 Linear Gate Stretcher.

PA 68 D.M. Patterson and J.G. Cramer, Phys. Lett. 27B, 373 (1968).

PE 69 F. Petrovitch, H. McManus, V.A. Madsen, and J.A. Atkinson, Phys. Rev. Lett. 22, 895 (1969).

PE 70 F. Petrovitch, private communication.

PE 71 F. Petrovitch, Thesis (Michigan State University, 1971) unpublished.

RA 68 J. Raynal, Nucl. Phys. A117, 101 (1968).

RA 71 J. Raynal, Proc. 3rd Int. Symp. on Polarization Phenomena in Nuclear Reaction, pp 687, University of Wisconsin Press, Madison (1971).

RI 64 B.W. Ridley and J.F. Turner, Nucl. Phys. 58, 497 (1964).

RY 70 R. Rybicki, T. Tamura and G.R. Satchler, Nucl. Phys. A146, 659 (1970).

SA 64 G.R. Satchler, Nucl. Phys. 55, 1 (1964).

SA 66 G.R. Satchler, Nucl. Phys. 77, 481 (1966).

SA 67 G.R. Satchler, Nucl. Phys. A92, 273 (1967).

SA 70 G.R. Satchler, Proc. 3rd Int. Symp. on Polarization Phenomena, Madison, (1970).

SA 71 G.R. Satchler, Phys. Lett., 35B, 279 (1971).

SC 64 F.H. Schmidt, R.E. Brown, J.B. Gerhart and W.A. Kolasinski, Nucl. Phys. 52, 353 (1964).

SC 69 R. Schaeffer, Thesis, Orsay, (1969); Report CEA - R - 4000.

SH 67 H. Sherif, Thesis (University of Washington, 1967) unpublished.

SH 68 H. Sherif and J.S. Blair, Phys. Lett. 26B, 489 (1968).

SH 70 G.G. Shute, Angular Correlations Associated with Coupled Equations, University of Melbourne, UM - P - 69 / 13 (1970).

SN 66 J.L. Snelgrove and E. Kashy, Nucl. Inst. Methods 52, 153 (1966).

SW 71 W.E. Sweeney, Jr. and J.L. Ellis, (to be published).

TO 61 W. Tobocman, Theory of Direct Nuclear Reaction (Oxford University Press, 1961).

TR 70 G.F. Trentelman and E. Kashy, Nucl. Inst. Methods 82, 304 (1970).

TU 64 J.F. Turner, B.W. Ridley, P.E. Cavanagh, G.A. Gard and A.G. Hardacre, Nucl. Phys. 58, 509 (1964).

WI 71 M.A.D. Wilson and L. Schecter, Phys. Rev. C4, 1103 (1971).